ELEMENTA
Science of the Anthropocene

Macfarlane, AR, et al. 2023. Evolution of the microstructure and reflectance of the surface scattering layer on melting, level Arctic sea ice. *Elem Sci Anth*, 11: 1. DOI: https://doi.org/10.1525/elementa.2022.00103

RESEARCH ARTICLE

Evolution of the microstructure and reflectance of the surface scattering layer on melting, level Arctic sea ice

Amy R. Macfarlane[1,*], Ruzica Dadic[1,2], Madison M. Smith[3], Bonnie Light[3], Marcel Nicolaus[4], Hannula Henna-Reetta[5], Melinda Webster[6], Felix Linhardt[7], Stefan Hämmerle[8], and Martin Schneebeli[1]

The microstructure of the uppermost portions of a melting Arctic sea ice cover has a disproportionately large influence on how incident sunlight is reflected and absorbed in the ice/ocean system. The surface scattering layer (SSL) effectively backscatters solar radiation and keeps the surface albedo of melting ice relatively high compared to ice with the SSL manually removed. Measurements of albedo provide information on how incoming shortwave radiation is partitioned by the SSL and have been pivotal to improving climate model parameterizations. However, the relationship between the physical and optical properties of the SSL is still poorly constrained. Until now, radiative transfer models have been the only way to infer the microstructure of the SSL. During the MOSAiC expedition of 2019–2020, we took samples and, for the first time, directly measured the microstructure of the SSL on bare sea ice using X-ray micro-computed tomography. We show that the SSL has a highly anisotropic, coarse, and porous structure, with a small optical diameter and density at the surface, increasing with depth. As the melting surface ablates, the SSL regenerates, maintaining some aspects of its microstructure throughout the melt season. We used the microstructure measurements with a radiative transfer model to improve our understanding of the relationship between physical properties and optical properties at 850 nm wavelength. When the microstructure is used as model input, we see a 10–15% overestimation of the reflectance at 850 nm. This comparison suggests that either a) spatial variability at the meter scale is important for the two in situ optical measurements and therefore a larger sample size is needed to represent the microstructure or b) future work should investigate either i) using a ray-tracing approach instead of explicitly solving the radiative transfer equation or ii) using a more appropriate radiative transfer model.

Keywords: Sea ice, Albedo, Ice-optics, Surface scattering layer, Radiative transfer model, Micro-computed tomography

1. Introduction

The 2019 IPCC special report on the ocean and cryosphere in a changing climate states that sea-ice albedo feedback is a key driver of sea-ice loss (Perovich and Polashenski, 2012; Poürtner et al., 2019). However, a lack of process understanding makes differentiating between anthropogenic and natural drivers of summer Arctic sea ice variability a challenge (Serreze et al., 2016; Ding et al., 2017; Meehl et al., 2018). We currently understand that the high reflectivity of sea ice exerts a large cooling influence on the Arctic system (Thackeray, 2019). Nevertheless, global climate models have highly variable representations of the sea-ice albedo feedback (Winton, 2006; Flanner et al., 2011; Colman, 2013), which contributes to uncertainty in climate projections. These variabilities come from spatial and temporal heterogeneity in surface conditions (including sea-ice properties, snow cover, and albedo; Su et al., 2015). Our understanding of Arctic sea-ice melt processes needs to advance to improve projections of sea-ice conditions.

The sea-ice extent at the end of the summer of 2020 was the second lowest in the satellite record

[1] WSL Institute for Snow and Avalanche Research, Davos Dorf, Switzerland
[2] University of Wellington, Kelburn, Wellington, New Zealand
[3] Polar Science Center, Applied Physics Laboratory, University of Washington, Seattle, WA, USA
[4] Alfred-Wegener-Institut, Helmholtz-Zentrum für Polar- und Meeresforschung, Bremerhaven, Germany
[5] Finnish Meteorological Institute, Helsinki, Finland
[6] Geophysical Institute, University of Alaska Fairbanks, Fairbanks, AK, USA
[7] Kiel University, Kiel, Germany
[8] SCANCO Medical AG, Wangen-Brüttisellen, Switzerland

* Corresponding author:
Email: amyrmacfarlane@gmail.com

(Perovich et al., 2020), continuing the trend in the recent sea-ice decline. A Siberian heat wave in the spring of 2020 initiated an early Arctic sea-ice melt (Meier et al., 2021), resulting in the melt season lasting more than a month longer than usual, with July and August 2020 being, on average, the all-time warmest and wettest months (Rinke et al., 2021). During the same year, the Multidisciplinary drifting Observatory for the Study of Arctic Climate (MOSAiC) expedition was moored alongside an ice floe in the transpolar drift stream collecting measurements (Krumpen et al., 2021; Nicolaus et al., 2022). The interdisciplinary approach allowed for the comparison of many measurement techniques and for experts in various research fields to work simultaneously on sea ice. This holistic approach allowed novel combinations of instruments to be installed and used on sea ice to better understand the influence of changes in the Arctic on sea-ice processes.

In the Arctic, the melt season conditions cause the highly reflective snow to melt, exposing bare sea ice to solar radiation. As a result of the absorption of this solar radiation, a porous, granular, and highly fragile pillared structure begins to form at the top of the melting sea ice. Here we refer to this surface structure as the surface scattering layer (SSL). The surface type is known as melting "bare ice," "white ice," or "loose, large ice grain layer" in the literature (Untersteiner, 1961; Maykut and Untersteiner, 1971; Grenfell and Maykut, 1977; Light et al., 2008; Malinka et al., 2016; Perovich, 2017; Light et al., 2022; Smith et al., 2022). Unlike snow, the origin of the SSL is not atmospheric but melting sea ice. The SSL governs the optical properties of summer sea ice due to its effective backscattering of solar radiation, which keeps the surface albedo relatively high (Maykut and Untersteiner, 1971). As a result, the SSL plays a vital role in the energy budget of melting sea ice and determines the surface melt of Arctic sea ice during summer (Smith et al., 2022). Despite the importance of the SSL for optical properties, there is no quantitative description of the evolution of the pore microstructure during melt (Petrich and Eicken, 2010), as the microstructure of the SSL has been challenging to measure in detail.

Measurements of the SSL microstructure previously relied on transporting the ice sample from its area of origin to a suitable laboratory to study its properties without structural change. Light et al. (2008) describe the SSL as an "intricate skeletal structure of fragile ice crystals." Because the SSL exhibits such a fragile structure, transporting it without structural change is difficult. Therefore, due to its high porosity and fragility, the microstructure of the SSL has not previously been measured in situ. Measuring the SSL in situ has previously been impossible without implementing an adopted method of casting (Lombardo et al., 2021).

Prior measurements were focused primarily on thickness and images of the surface. We know that the thickness of the SSL varies spatially between approximately 0.01 and 0.10 m (Light et al., 2008; Perovich, 2017). For this study, we define the SSL as the surface structure with densities below 700 kg m^{-3}. This threshold slightly exceeds the threshold for firn (Britannica, 2014). Due to the vertical structural arrangement and increase in density, using a ruler to penetrate the structure to lower depths and measure the complete thickness of the SSL is challenging. Without manually removing the SSL, however, the SSL thickness is often underestimated (Smith et al., 2022). Future work to obtain a better measurement of the SSL thickness would benefit from using a shovel to remove the surface layer to the greatest depth that is physically feasible. Through ice cores, we know that a large proportion of the volume of Arctic sea ice is composed of granular and columnar ice. The latter has pore space elongated along the vertical (Eicken, 2003; Huang et al., 2016; Oggier and Eicken, 2022), which informs our understanding of the surface microstructure during the melt season. During the melt, a liquid film grows along the grain boundaries, which then causes more melt in these areas. This process is nicely visualized in figure 2 in Dash et al. (2006). The elongated pore space, gravity drainage of surface water, and internal melt along the vertically elongated grain boundaries (Cole and Shapiro, 1998; Freitag and Eicken, 2003) likely explain the pillared structure of the SSL.

Below the SSL lies the drained layer (DL). DL thickness is limited to the difference between the freeboard height and the SSL thickness. Perovich (2017) notes a DL thickness ranging from 5 to 30 cm. Densities of the DL lie within the range of densities for the underlying interior ice (IL), 700–900 kg m^{-3}. The only difference between these two categories (DL and IL) is that the DL depends on the freeboard height, and the meltwater drains away by gravity, leaving airspace and higher scattering. As the surface undergoes melt, the SSL is ablated, and the DL undergoes preferential crystal boundary melt, which causes the porosity to increase and the DL to transition into the new SSL. The seasonal evolution of these layers is shown in the schematic in **Figure 1**. The porosity of these layers is due to different internal processes: the SSL has a high porosity (density range of approximately 0–700 kg m^{-3}) due to preferential grain boundary melt (Dash et al., 2006); the DL porosity is due to brine channel drainage and pathways forming for brine and meltwater (Petrich and Eicken, 2017). Finally, the IL porosity is due to brine channels within the columnar ice (with IL density of approximately 700–900 kg m^{-3}, which decreases throughout the summer; Frantz et al., 2019). During melt, wet snow metamorphism and surface ablation cause freshwater infiltration through the SSL and DL pore spaces. We can assume that shortwave radiation is producing grain boundary melt at the surface and causing an increase in porosity. However, because shortwave radiation intensity decreases at lower levels within the ice structure, another mechanism must cause the increase in porosity. At these lower levels, the increased porosity is therefore attributed to brine channel conditions.

The high light scattering of the SSL is responsible for the consistently high albedo and relatively low transmittance of bare, melting sea ice (Light et al., 2008; Light et al., 2015). Surface melt and constant regeneration of the SSL layer produce a consistently high albedo during the Arctic summer (Perovich, 2002; Grenfell et al., 2006; Light

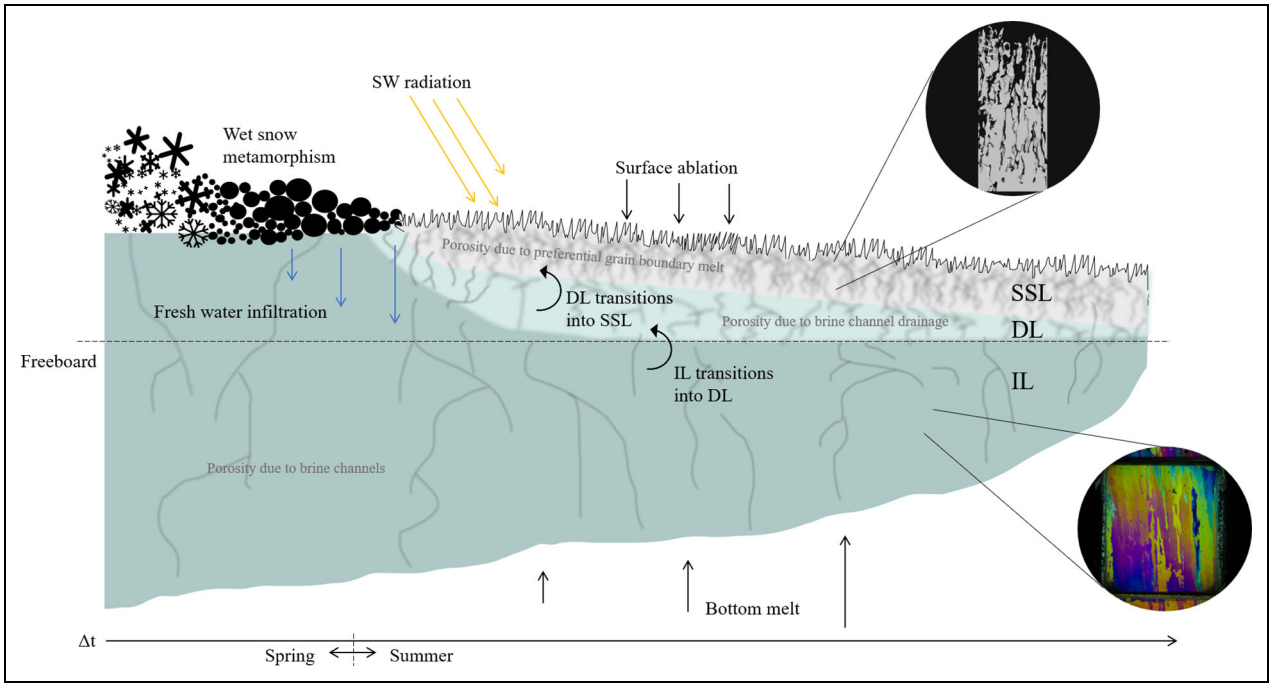

Figure 1. Schematic of the formation of the surface scattering layer (not drawn to scale). This schematic represents the surface scattering layer (SSL) formation from the beginning of the snowmelt in spring through the end of summer, with time (Δt) represented along the x-axis. Wet snow metamorphism and surface ablation cause freshwater infiltration through the pore spaces of the SSL, drained layer (DL) and interior layer (IL) during the melt. Once the snow melts and drains away, surface ablation maintains the SSL thickness. The SSL persists because of two processes: (1) surface ablation due to incoming shortwave (SW) radiation (reducing SSL thickness), and (2) the transition of IL to DL to SSL (increasing SSL thickness). DL thickness is the freeboard minus SSL thickness. This schematic shows the changing freeboard due to a reduction in the ice thickness. A thin section of columnar ice taken on the MOSAiC expedition (bottom) and a microCT SSL microstructure (top) can be seen in the circular insets.

et al., 2021). Therefore, the SSL plays a crucial role in the energy balance of sea ice during the melt season. Light et al. (2022), in comparing data from MOSAiC and the Surface Heat Budget of the Arctic Ocean (SHEBA) expedition, confirmed that "the spectral albedo for bare, melting sea ice also appears invariant with respect to the ice age (first-year, second-year, multi-year). We suggest that the principal reason for this invariance is the ubiquitous presence of surface scattering layers." This suggestion notably excludes sedimented areas. Throughout this manuscript, albedo represents the integrated hemispherical spectral albedo, and reflectance refers to the reflectivity of an artificially illuminated surface. Measurements of sea ice albedo and reflectance are most informative when combined with observations of the physical properties of the SSL and not simply its thickness, as the thickness is often underestimated when measured by a ruler (as previously explained). Light et al. (2022) advised that observations should include surface type description, snow and ice thickness, snow grain size and density, ice freeboard, temperature, and texture.

Until now, measurements of the microstructure of the SSL have not been made. Radiative transfer models (RTMs) have been used to infer the microstructure of the ice surface from optical measurements (Grenfell, 1991; Ehn et al., 2008; Light et al., 2008; Light et al., 2015; Malinka et al., 2016; Perovich, 2017). Inherent optical properties (IOPs) include those fundamental to modelling the ice albedo: scattering and absorption coefficients and scattering phase functions. Previously IOPs of melting sea ice have been inferred or measured in the laboratory (Grenfell and Perovich, 1981; Moritz and Light, 2014). Our limited knowledge of the geometrical structure and impurity content of the ice and snow means that RTMs are limited by knowledge of the IOPs (Light et al., 2008).

In this study, we investigated the evolution of the microstructure and reflectance of the SSL on melting, level Arctic sea ice. We addressed the questions: What are the geometrical properties of the SSL? How does the SSL vary spatially and temporally? What are the optical properties of the SSL? How does the spatial and temporal variability affect the optical properties? To answer these questions, we have made the first microstructural measurements of the SSL for the summer melt season. We introduced and used a novel instrument that houses a near-infrared camera (NIRbox) to measure reflectance under standardized conditions and compared results to the commonly used analytical spectral device (ASD). We combined the microstructural information with albedo and reflectance to test if spatial variability of the surface structure influences reflectance. By using microstructural measurements as inputs to a radiative transfer model, we could directly compare measured and modelled reflectance at 850 nm.

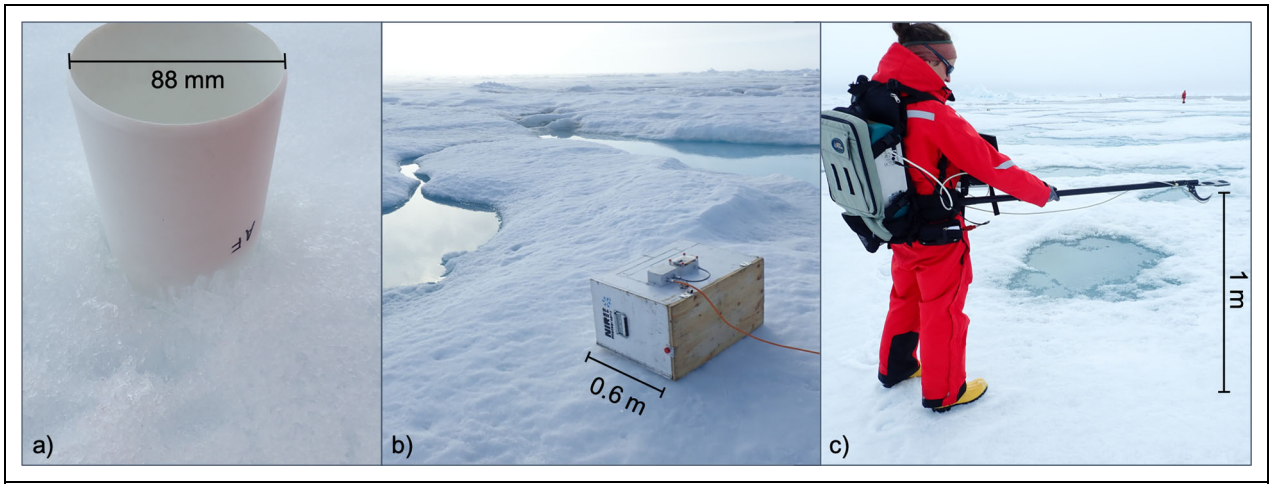

Figure 2. Methods for in situ measurements of the surface scattering layer. The three instruments used throughout the summer months of the MOSAiC expedition to document the geometric and optical properties of the surface scattering layer (SSL): (a) an X-ray micro-computed tomography (microCT) sample measuring the geometry; (b) a novel, near-infrared instrument (NIRbox) pointing down to image the SSL at 850 nm; and (c) an analytical spectral device (ASD) taking spectral albedo measurements of the SSL. Scale bars indicate the different footprints of each instrument (microCT = 5.03×10^{-3} m^2, ASD = approximately 1.77 m^2, NIRbox = 0.12 m^2). Images from Macfarlane et al. (2022c).

2. Methods

Measurements of SSL density, specific surface area (SSA, total surface area of a material per unit of mass), spectral albedo and reflectance at 850 nm (NIRbox; see Section 2.3) were taken during the MOSAiC expedition (Nicolaus et al., 2022) using techniques applied to the study of snowpits in winter (Macfarlane et al., 2021). We used the same suite of measurements for the SSL analysis as used for the snowpits in winter. This study is focused on the summer months, but as it represents a continuation of the winter measurements, we continue to use terminology such as snowpit. Between June and July 2020 (Leg 4), there was remnant coarse snow adjacent to the ridges, but the level ice became snow-free, and only the SSL was present. For this study, we define the surface of melting sea ice as the origin ($z = 0$). All of the measurements in this study were made within the Central Observatory of the expedition ice camp, a designated floe area close to the research vessel *Polarstern* (Knust, 2017), with a diameter of approximately 1 km and a mixture of level seasonal and level second-year ice. We focused this study on level ice and excluded ridged or heavily sedimented areas of the floe. These heavily sedimented areas were in noticeable patches with clean areas in between. Areas with impurities that were not visible were not influencing the absorption of the wavelength used in this study (850 nm). We chose the measurement locations on arrival at the floe, set up undisturbed areas and repeatedly measured the SSL at snowpit sites (location details in Figure S1). Additional measurements were made along transects to quantify spatial variability, which was not necessarily represented by the dedicated undisturbed areas. The frequency of SSL measurements was weekly or twice a week. The X-ray micro-computed tomography (microCT) samples (**Figure 2a**) and the reflectance measurements from the near-infrared camera (NIRbox; **Figure 2b**) were collected as part of the "snowpit" dataset (Macfarlane et al., 2021). Measurements of spectral albedo using the ASD (optics-RB/LDL/Eco/Stern; Figure S1) were co-located both along part of the transects and at individual snowpits within the undisturbed areas (Smith et al., 2021; **Figure 2c**). Co-located samples were taken at the same time. However, due to the destructive sampling of the microCT, the locations were not precisely aligned but side by side. Samples that were not co-located were taken at different times and areas within the Central Observatory.

2.1. Theory

The backscattering of near-infrared radiation depends on the SSA of snow and the SSL (Wiscombe and Warren, 1980; Dozier, 1992). At 850-nm wavelength, the microstructure of different snowpacks and SSL can be distinguished because the absorption of near-infrared radiation within the ice is higher than that of visible radiation within the ice (Matzl and Schneebeli, 2006). As a result, 850 nm is sensitive to the SSL and the underlying DL, explaining why it is the optimal wavelength for this study and previous studies on snow microstructure (Matzl and Schneebeli, 2006). Impurities at low concentrations do not influence the reflectance of snow/SSL in the near-infrared spectrum (Wiscombe and Warren, 1980; Leroux et al., 1999); therefore, we do not model impurities in this study. The radiative transfer equation is composed of scattering and absorption coefficients. We kept the absorption term constant by focusing on the 850-nm wavelength. We only varied the scattering term when we investigated how the geometrical input parameters influence albedo. These input parameters included the density, SSA and thickness calculated from each microCT sample. Using 850-nm albedo as an output allowed for

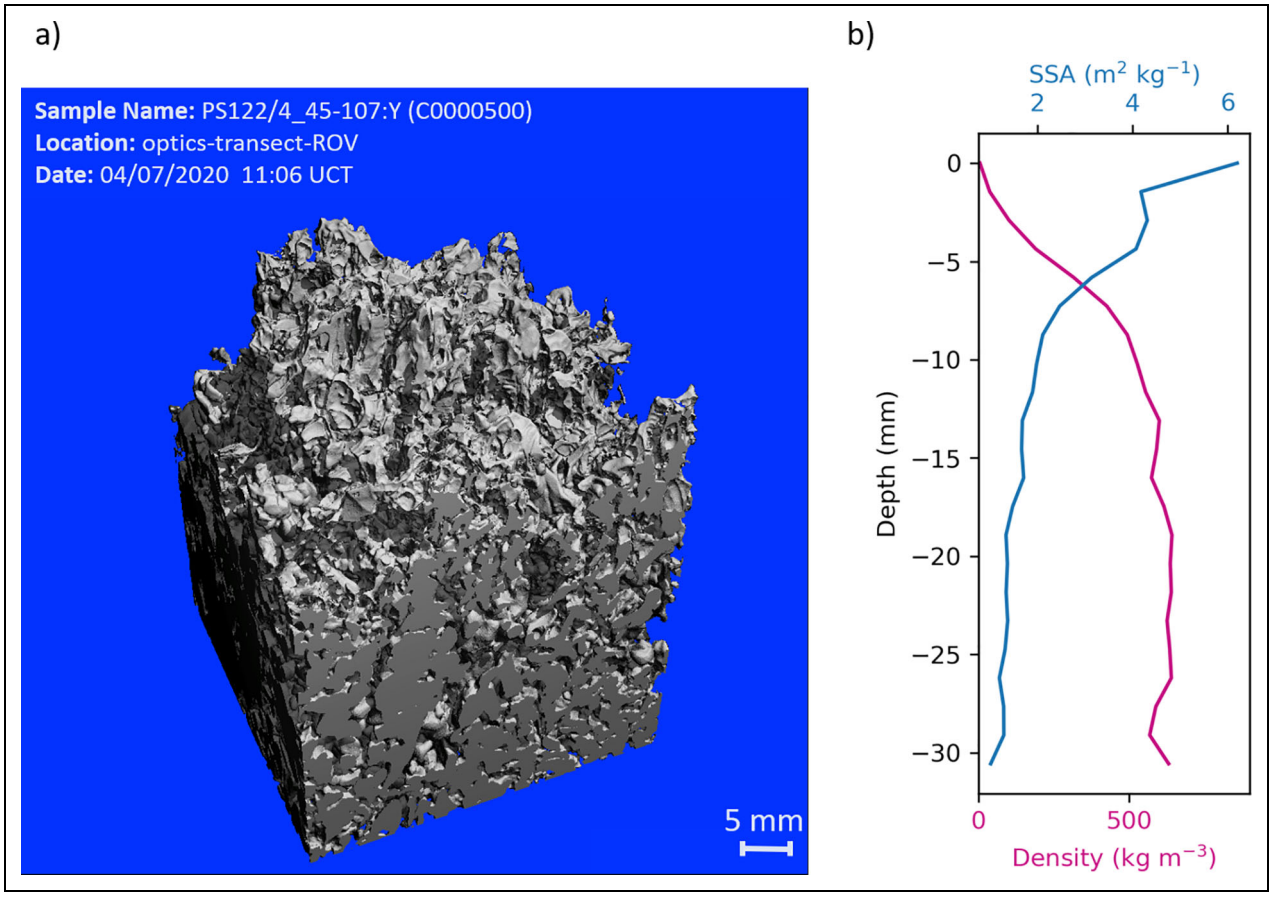

Figure 3. A 3-D model reconstruction of the surface scattering layer and corresponding microstructural profiles. (a) 3-D model reconstruction from a micro-computed tomography sample taken on July 4, 2020, at the Central Observatory optics-transect-ROV site. (b) Profiles of the corresponding microstructural parameters of density and specific surface area (SSA).

intercomparison between the measured (ASD and NIRbox) and modelled reflectance (microCT/TARTES).

2.2. Microstructure measurements

Fifty-four cylindrical SSL samples (**Figure 2a**) of 55 to 80 mm in diameter and a height of 100 mm were collected in the field using a hollow drill bit. This method allowed us to keep the microstructure intact while also sampling the underlying DL. To account for any microstructural damage at the edges of the samples, we analyzed a sub-sample of volume commonly 20 × 20 mm in width. A sub-sample volume is reconstructed in **Figure 3**, with more examples provided in Figure S2. The samples were drained to the irreducible water content during extraction and transferred to a sample holder. The samples were immediately transported to a cold laboratory at −15°C to prevent structural changes to the SSL prior to measuring it. The SSA was not affected when the sample was frozen, as any liquid water had percolated out of the sample. Freezing of the pore water was unlikely due to the melting state of the sea ice reflected in its large pore sizes. The average salinities of the samples in July were 0 ppm (Macfarlane et al., 2021), and the average temperature at the time of sample collection in July was 0.3°C (Macfarlane et al., 2021).

The microstructure of the SSL was measured on-site by installing a microCT in the cold laboratory onboard the *Polarstern* and scanning the samples within 24 h of collection. Micro-computed tomography is a 3-D imaging technique using X-rays to image cross-sections of an object and to reconstruct a 3-D model of that object (Scanco, 2019); in our case, an SSL sample. The −15°C cold laboratory and an actively ventilated microCT meant that the temperature inside the microCT was consistently −12°C during the scan. This consistency was due to the good ventilation system. The internal temperature of the microCT was displayed during the scan and checked often. The samples were scanned, and using this sampling collection method, we could measure the microstructure to a resolution of 26–42 µm in an approximate 20 × 20 mm footprint, depending on the sample diameter. Because a sample maintains its microstructure at −12°C, a second scan of the same sample would have shown no change. After scanning the samples and producing the 3-D model reconstruction, we segmented the voxels of ice and air within the 3-D structure and used the segmented images to calculate the geometrical parameters of the SSL. We used IPL Version 5.42 (Scanco Medical AG) to evaluate density, SSA, and optical equivalent diameter (d_{eff}) using a triangulation-based estimate from the microCT samples

(Hildebrand and Rüegsegger, 1997). The term d_{eff} is the diameter of a sphere of equivalent volume to that of the irregular-shaped ice grains and was calculated as $d_{eff} = 6/\rho_{ice} \cdot SSA$, where ρ_{ice} is the density of ice, and SSA has units of mm^{-1}. These three parameters were chosen, as the density and SSA or d_{eff} are necessary inputs into RTMs. SSA and $d_{eff,}$ can be used interchangeably due to their inverse relationship; for the rest of this manuscript, we focus on SSA. The amount of reflected and absorbed visible and near-infrared solar radiation depends strongly on the SSA, a parameter essential for remote sensing applications (Gergely et al., 2014). A typical sample is shown in **Figure 3**, with additional samples provided in Figure S2.

2.3. Reflectance measurements at 850 nm

Near-infrared photography is a method of determining the SSA of snow and the stratigraphy of alpine snowpacks (Matzl and Schneebeli, 2006). The new NIRbox is a modification of the method developed by Matzl and Schneebeli (2006) by artificially illuminating the surface with two LED lamps at 850-nm wavelength in a lightproof box (**Figure 2b**) and using a MAPIR camera (Survey3 N MAPIR Camera: Near Infrared) to image the snow surface. It is a low-cost, accurate measurement made at wavelengths relevant for microstructure. In this study, we used the NIRbox to measure the surface reflectance at 850 nm, obtaining 78 surface reflectance images of the SSL. We placed the lightproof box facing down on the ice surface so that the camera could capture the surface reflectance of the lights with no outside influence from incoming radiation, cloud cover, surface inclination or azimuth angle due to its ease of use. This setup allowed the NIRbox to be used throughout the expedition during the polar day and night. For measurements taken during the polar day, a picture without the illumination of the lights inside the box was taken before each measurement and used as a reference to ensure that no external light was entering the box from the underlying ice or the edges of the box. The NIRbox images have a footprint of 0.12 m^2 and a resolution of 0.18 mm to capture the macro-scale variability of the surface microstructure. The TIFF images (Macfarlane et al., 2022a) were calibrated against targets with reflectances of 95% and 50% inside the box and corrected for inhomogeneous illumination. The camera was not monochrome and had RGB channels. The red channel was used for this study, but any RGB channel could have been chosen. The correction was done by dividing the red channel of the image by the normalized red channel of the reference plate image. The greyscale of this image was smoothed with a 2-D Gaussian mask. From the smoothed image, the target reflectance values of 95% and 50% reflectance were identified. After selecting the targets manually and identifying the reflective values of the targets of known reflectance, images were calibrated by multiplying the corrected image by $\frac{1}{2}\left(\frac{0.95}{mean(ref95)} + \frac{0.5}{mean(ref50)}\right)$, where *ref*95 and *ref*50 are the reflectances of the 95% and 50% targets, respectively. These calibrated images were saved, and the mean surface reflectance of each NIRbox image (NIR_{850}) was measured by averaging the reflectance of each pixel within a sub-volume. The sub-volume of these images excludes the frame and targets. These output images are an aggregation of the small-scale variability in reflectance in the images resulting from the microstructure. This study uses mean surface reflectance only. **Figure 4** shows examples of the NIRbox images of the SSL alongside the histograms of the reflectance values.

Spectral albedo was measured using an Analytical Spectral Device FieldSpec3 spectroradiometer (Smith et al., 2021; Light et al., 2022). We calculated the albedo using the incident-to-reflected flux ratio for wavelengths of 350–2500 nm. This study focuses on the 850-nm wavelength to compare ASD and NIRbox reflectance. ASD albedo measurements have a footprint of approximately 1.77 m^2. The measured reflectance of the ASD at 850 nm is represented by ASD_{850}. More details about the ASD instrument, collection methods and quality control process can be found alongside the published dataset (Smith et al., 2021). By comparing the two methods (NIR and ASD) we could test the novel NIRbox measurement device. A time series of the two measurements is shown in **Figure 5a**.

2.4. Two-streAm Radiative TransfEr in Snow (TARTES)

Geometry (SSA, density, and layer thickness) from the microCT SSL samples (Macfarlane et al., 2022b) were used as input into the Two-streAm Radiative TransfEr in Snow model (TARTES 1.0; Libois et al., 2013; Libois et al., 2014). TARTES is based on the delta-Eddington approximation (Joseph et al., 1977) and uses measured physical properties in a multi-layer snowpack to compute the spectral albedo and irradiance profiles. Instead of a multi-layered snowpack, we used the layered SSL and the DL, where each horizontal layer is assumed to have homogeneous physical characteristics. TARTES was chosen due to its ease of use and well-documented code. We tested different layer segmentation of the microCT samples of the SSL to find the optimal layering. The layering setup ranged from one layer, three layers of equal thicknesses, weighted three layers with varying thicknesses, and five layers of equal thicknesses. Layers were weighted by taking the sum of the total SSA of the sample and dividing it by the required layers (for this study, three layers were chosen). This approach meant that each layer had equal sums of the SSA, as seen in Equation 1. The number of slices corresponding to a given layer is represented by n in Equations 1 and 2. The number of slices was multiplied by the slice height (Δz) to give the height of each layer ($height_{L1} = n_{L1} \cdot \Delta z$).

$$\frac{1}{3} \cdot \sum_{n=1}^{n_{tot}} SSA_{tot} = \sum_{n=1}^{n_{L1}} SSA_{L1} = \sum_{n=1}^{n_{L2}} SSA_{L2} = \sum_{n=1}^{n_{L3}} SSA_{L3} \quad (1)$$

$$\begin{aligned} sample\ height &= n_{tot} \cdot \Delta z \\ &= n_{L1} \cdot \Delta z + n_{L2} \cdot \Delta z + n_{L3} \cdot \Delta z \end{aligned} \quad (2)$$

This approach of weighting the layers ensured that if there were higher SSA values at the surface, we would use a smaller layer to avoid missing the details in the model,

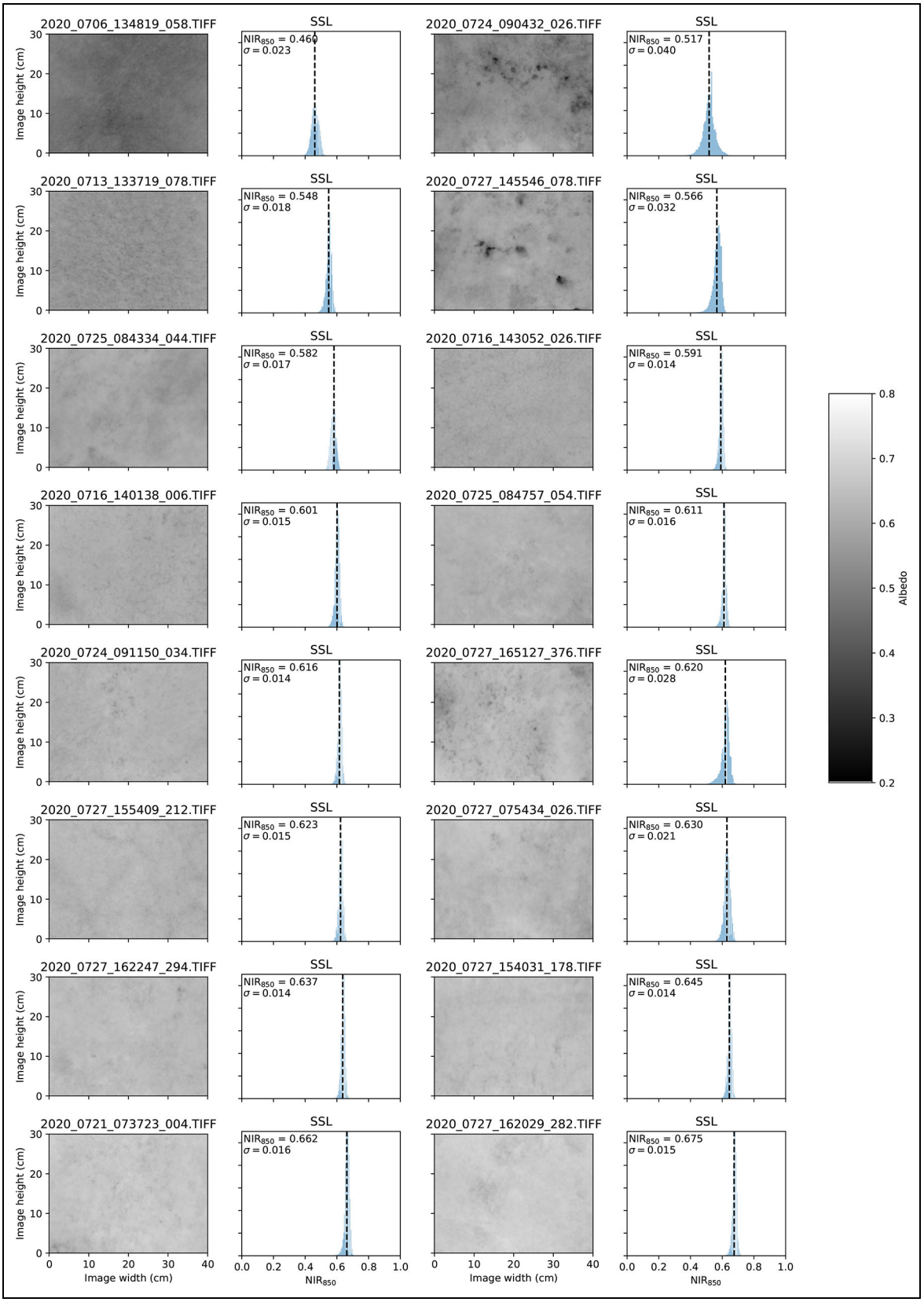

Figure 4. A selection of NIRbox images with their corresponding histograms. Spatial variability of the sea ice surface is shown in the near-infrared reflectance range at 850 nm (NIR_{850}). All images were taken in July 2020 within the Central Observatory. The date of each image appears in the filename; e.g., "2020_0713_" is July 13, 2020. Histograms of the reflectances can be seen to the right of the NIRbox image. NIR_{850} and σ indicate the mean and standard deviation, respectively, of the reflectance of the area shown in the image (number of pixels = 1700 × 2250). TIFF images are available in Macfarlane et al. (2022a).

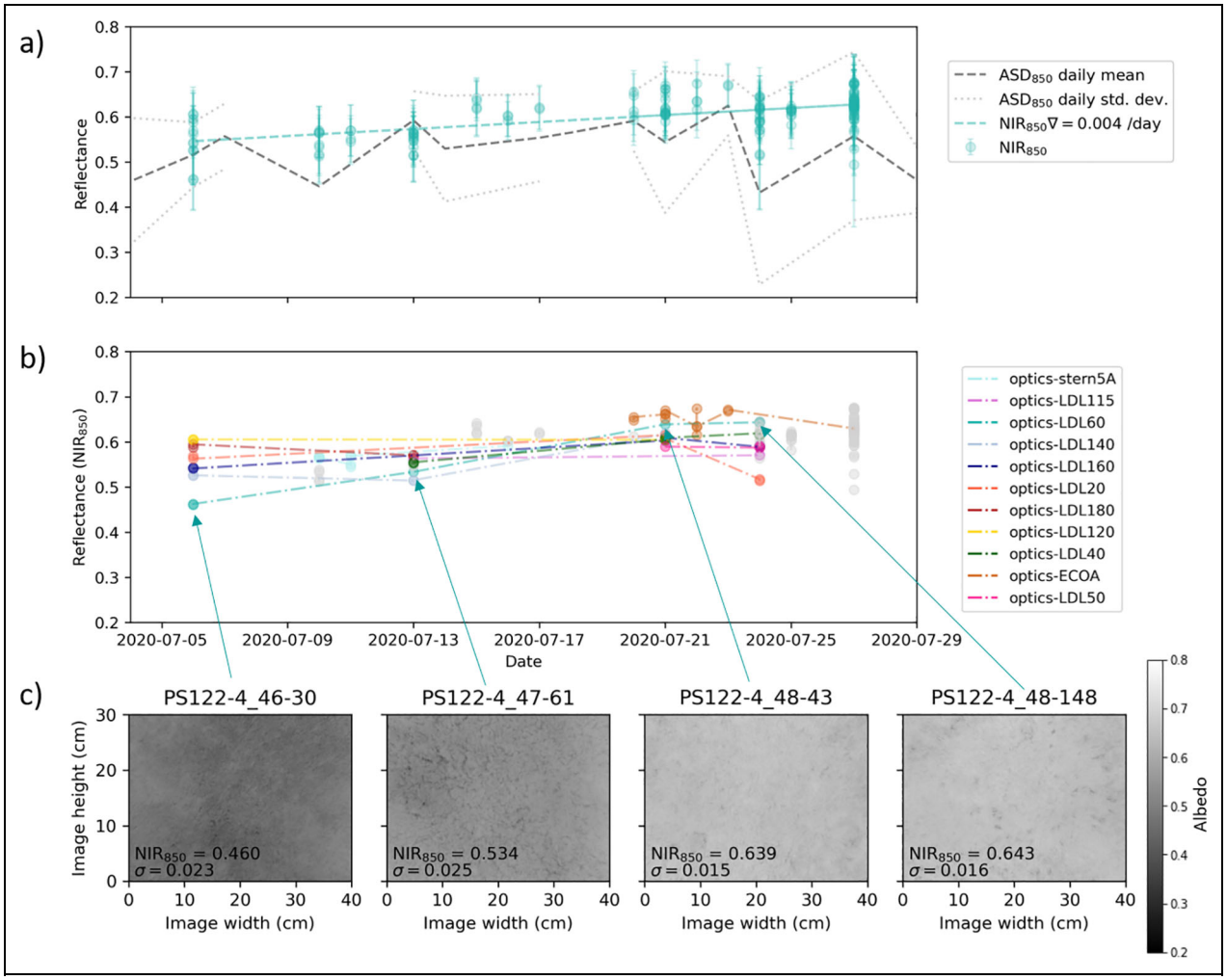

Figure 5. Time series of reflectance measurements from the analytical spectral device and NIRbox images. Reflectance measurements at 850 nm from the analytical spectral device (ASD_{850}) and the NIRbox images (NIR_{850}) over the month of July. In (a), a time series of the mean ASD (dark grey line) with one standard deviation is indicated by the light grey lines plotted alongside the average reflectance of the NIRbox image pixel values. The ASD_{850} daily mean does not show a continuous line, as the spectral albedo was not measured every day. Error bars plotted with the NIR_{850} data points are one standard deviation of all the pixels in the NIRbox image. All of these measurements were taken in the Central Observatory on a mixture of second-year and seasonal ice. The NIRbox and ASD were often measured in the same location; however, this figure also includes measurements that were not co-located. In (b), the time series of these NIRbox images for the month of July are grouped by location. Each colour shown in the inset legend indicates a unique location with lines connecting measurements at the same location. Grey points indicate one-off measurements that are not part of a time series. In (c), a collection of four NIRbox images is shown from Optics-LDL60, the location in (b) showing the largest increase in reflectance over the period. The dates in 2020 (and file names) of the images, left to right, are July 6 (2020_0706_134819_058.TIFF), July 13 (2020_0713_131206_016.TIFF), July 21 (2020_0721_140144_094.TIFF) and July 24 (2020_0724_091952_054.TIFF). These TIFF images are available in Macfarlane et al. (2022a).

and the vertical distribution of the observed SSA would be better represented. By testing multiple layers, we found that one layer produces a higher albedo than a weighted three-layer. A five-layered approach with equal layer thickness and a weighted three-layer approach had the same albedo values. For the remainder of this study, the weighted three-layer approach was used, as less computational power is needed to model fewer layers.

The DL is located beneath the SSL. Some samples included some underlying DL due to the drilling collection method. A density of 700 kg m^{-3} was applied to the samples as the cut-off between the SSL and the DL to account for the inconsistent inclusion of the DL in the samples. An artificial layer representing the DL was added beneath the model SSL layers. Details of this layer are given below. Although the SSL and DL are described and modelled as distinct layers in this study, the transition is likely gradual in reality, as mentioned by Smith et al. (2022). This transition could be better represented in a different model setup, as explained in the discussion. Different thicknesses of the DL were tested in the model

at the start of this study. However, thicknesses beyond 300 mm had no influence on the output spectral albedo due to negligible transmission at 850 nm due to reflection at the surface and absorption in the DL. Therefore, the artificial DL layer in this study was 300 mm thick (to account for an approximate DL thickness relating to the freeboard of 2-m thick ice) and had an SSA of 0.1 m^2 kg^{-1} and a density of 700 kg m^{-3}. $TARTES_{850}$ represents the TARTES 850 nm output with a weighted three-layered microstructural input, an underlying artificial DL, and a subsurface albedo of 0.1. In the model, this subsurface is called "soil albedo."

An overestimation of radiative transfer models was also found by Dadic et al. (2013) when using RTMs in Antarctic blue ice areas. The bias increased with increasing SSA. The possible reasons were summarised, and the asymmetry factor g in the model was found to be the most plausible answer (Dadic et al., 2013). Throughout this study, we used a spherical shape with an asymmetric factor, $g = 0.895$, and an absorption enhancement parameter, $B = 1.25$. These parameters are explained further in Libois et al. (2014). We conducted a test to understand the influence of changing the asymmetry factor on the TARTES model output. The input layers for this test were simply a three-layered input, where layer one was the average of all SSL profiles of 0–20 mm (0.02 m, 332 kg m^{-3}, 4.08 m^2 kg^{-1}), layer two was the average of all profiles above 20 mm (0.05 m, 578 kg m^{-3}, 2.09 m^2 kg^{-1}), and the third layer was the modelled DL (1 m, 700 kg m^{-3}, 0.1 m^2 kg^{-1}) used earlier in this study.

3. Results

3.1. SSL microstructure

MicroCT microstructural measurements taken from the end of June through July within the MOSAiC Central Observatory were used to understand the properties of the SSL. The stable oxygen isotope signal of the SSL on level ice and excluding ridged areas in July 2022 was –7.3 ‰ ± 6.4 ‰ (one standard deviation, σ; Macfarlane et al., 2022d), indicating that we were measuring the SSL during this period and excluding melting snow. The average stable oxygen isotope signal for the SSL had a more negative value than ocean water. This result was expected, as we were measuring some second-year ice with possible refrozen melted snow from the previous winter. The average winter snowpack had an average of −18.5 ‰ ± 9.6 ‰ (σ). We were, therefore, outside one deviation of the isotopic signal of snow. A typical SSL structure can be seen in **Figure 3**. We took this SSL sample on July 4, 2020, at the optics-transect-ROV site (location can be seen in Figure S1). The SSA is highest at the surface and decreases with depth. The pillar-looking structures are visible in **Figure 3** (more sample cross-sections and density profiles can be seen in Figure S2).

Common patterns can be seen in the SSL microstructure. **Figure 6** shows all microCT SSL profiles plotted for density, SSA and optically equivalent diameter (d_{eff}). All profiles have a low (high) density and d_{eff} (SSA) at the surface, which increases (decreases) with depth. After a gradual density increase in the top 20 mm, the density is highly variable between samples; in the lower depths, it varies between 300 and 700 kg m^{-3}. This pattern and variability are also seen when we plotted the depth where the density threshold (700 kg m^{-3}) was reached (left scatter plot in **Figure 6**). This scatter plot shows variability in the thickness of the samples ranging from 20 mm to 100 mm before the threshold is reached. The top 0–20 mm has a density of 332 ± 84 kg m^{-3} (σ, n = 51). After 20 mm, the gradient of the density profile appears to reduce to an average density of 579 ± 109 kg m^{-3} (σ, n = 51), which is the upper limit of the density of snow (Muskett, 2012). The SSA (middle) plot in **Figure 6** also shows high variability at the surface, with an average SSA at 0–20 mm of 4.08 ± 1.18 m^2 kg^{-1} (σ, n = 51) and a reduction of the gradient below 20 mm, where the average SSA is 2.09 ± 0.68 m^2 kg^{-1} (σ, n = 51).

The microstructure (density, SSA, depth) of the SSL, determined from microCT samples, appeared to show no change over the time period of sample collection (**Figure 7**). To test this, the full sample was split into three layers to better understand the consistent structure over the time period; these layers were later used for the TARTES model input. **Figure 7** shows that layer one has highly variable SSA and density, but their averages do not change over time. Values of the gradients of the layer two trendlines (provided in **Figure 7**) indicate that the depth of this layer increases by 0.16 mm per day, the density increases by 2 kg m^{-3} per day, and the SSA decreases by 0.008 m^2 kg^{-1} per day. A unit root test was conducted to determine if the time series variable is non-stationary and possesses a unit root. This test, called the Augmented Dickey-Fuller (ADF) test (Mushtaq, 2011), was performed on the dataset to determine how strongly the time series is defined by the trend. The null hypothesis is that this dataset is not stationary. The results of this test include the following ADF statistic for the layer two time series: −5.28 (depth), −5.17 (density), −4.45 (SSA), with corresponding p-values of 0.000006 (depth), 0.00001 (density), 0.0002 (SSA). The critical values for layer two at 1% are −3.58 (depth), −3.58 (density), and −3.58 (SSA). The more negative the ADF statistic, the more likely to reject the null hypothesis. For all three parameter time series, the ADF statistic is less than the value at 1%. This result suggests rejection of the null hypothesis with a significance level of less than 1% (i.e., a low probability that the result is a statistical fluke). Rejecting the null hypothesis means that the process has no unit root, and in turn, all three time series are stationary and do not have a time-dependent structure. This lack of temporal variability can be seen in the low gradients of the trendlines (**Figure 7**). To conclude, we can confidently state that the microstructure shows no temporal change.

3.2. SSL reflectance

Figure 4 shows examples of NIRbox images of 0.12 m^2 areas, taken in July 202, alongside histograms of the SSL surface reflectance. The mean NIR_{850} and one standard deviation (σ) are displayed in the histograms. These images have been corrected for inhomogeneous illumination and calibrated against the targets, as described in the

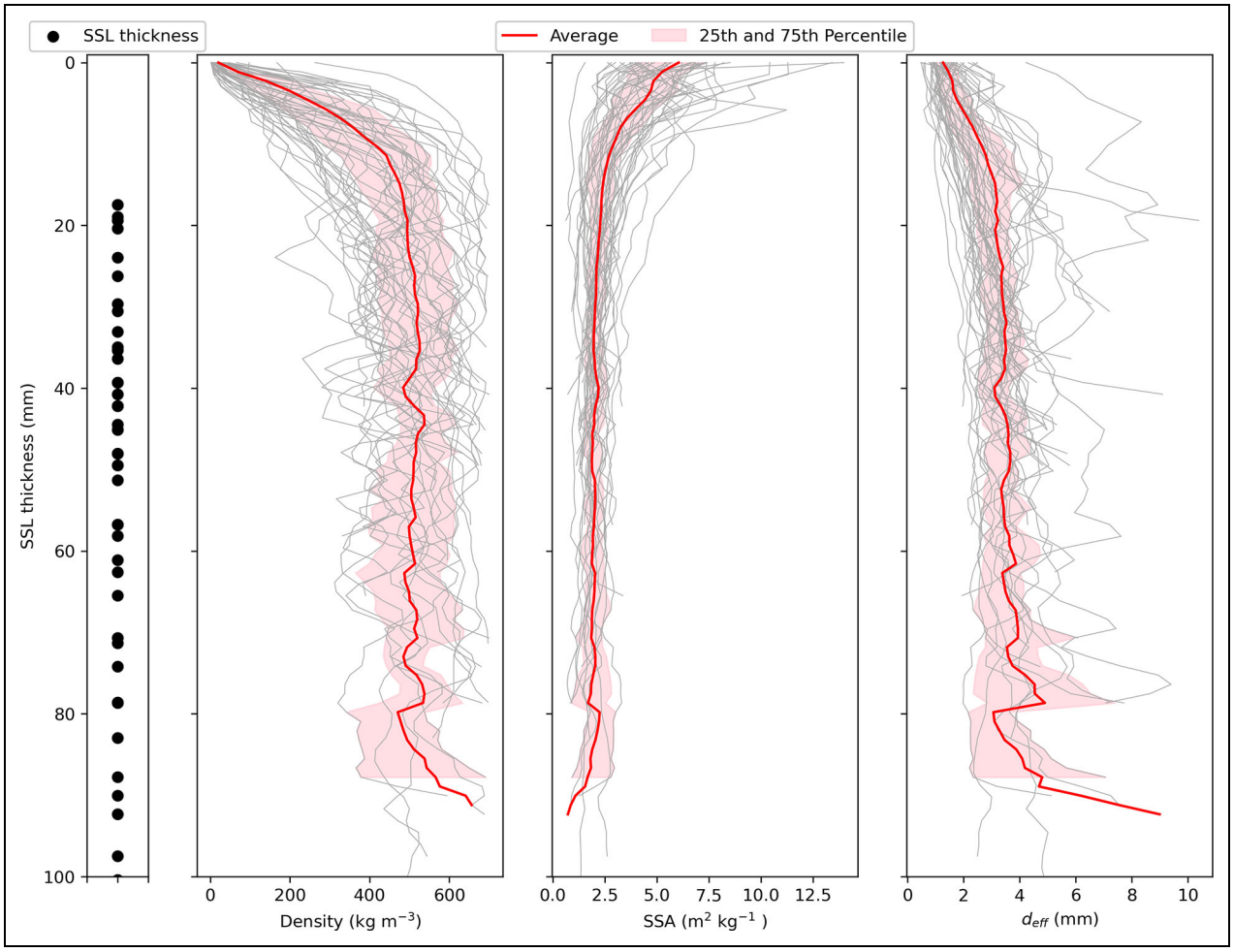

Figure 6. Profiles from all surface micro-computed tomography samples of melting summer sea ice. Profiles of density, specific surface area (SSA) and optically equivalent diameter (d_{eff}) for individual micro-computed tomography samples of the surface scattering layer (SSL) taken in June and July are plotted in grey. The average profile (red line) and the 25th and 75th percentiles (red-shaded areas) are displayed for each parameter. A cut-off density threshold of 700 kg m^{-3} was applied to account for inconsistent sampling of the underlying drained layer. The depths of the SSL after applying this threshold are plotted as black circles in the panel on the left.

methods section. The images can be used to visualize the spatial distribution of the SSL on level ice within the CO and to give an indication of the spatial variability within the NIRbox footprint. However, for this study, the means of images are used later to compare to the ASD. In the figure, the images with darker spots caused by drainage channels within the ice can be seen to lower the average mean reflectance and increase the standard deviation.

The reflectance of the ice surface shows no temporal change over the time period shown in **Figure 5a**, which compares the daily mean and one standard deviation of all ASD spectral albedo (ASD_{850}), and NIRbox measurements of the SSL at 850 nm (NIR_{850}) in July 2020. The error bars plotted with the NIR_{850} data points (one standard deviation of all the pixels in the NIRbox image) allow for a quantification of the spatial variability within the image. The NIR_{850} mean over this time period of 0.60 $\pm$ 0.04 (σ) is comparable to the ASD850 mean of 0.63 $\pm$ 0.09 (σ). The reflectance of the NIRbox images increases by 0.008 per day. As for **Figure 7**, the ADF unit root test was performed on this dataset to determine how strongly the time series is defined by the trend. The results for this test include the ADF statistic of -3.69, with a p-value of 0.004, and the critical value at 1% of -3.47. Because the ADF statistic is less than the value at 1%, we can reject the null hypothesis with a significance level of less than 1% (i.e., a low probability that the result is a statistical fluke) and conclude that the time series does not have a time-dependent structure.

Having returned to the same locations for measurements with the NIRbox allowed us to determine if there were any temporal changes in the NIR_{850} values for SSL reflectance. **Figure 5b** shows the same data as in **Figure 5a** but the data are grouped by location. The majority of locations showed no change during July 2020. However, the location designated Optics-LDL60 showed an increase in reflectance from 0.46 to 0.64 within 15 days. This increase could be due to drainage of surface water, although wetness was not measured in this study, or to changes in the microstructure.

Figure 8 displays this increase in reflectance in more detail. The NIRbox images in **Figure 8a** are co-located

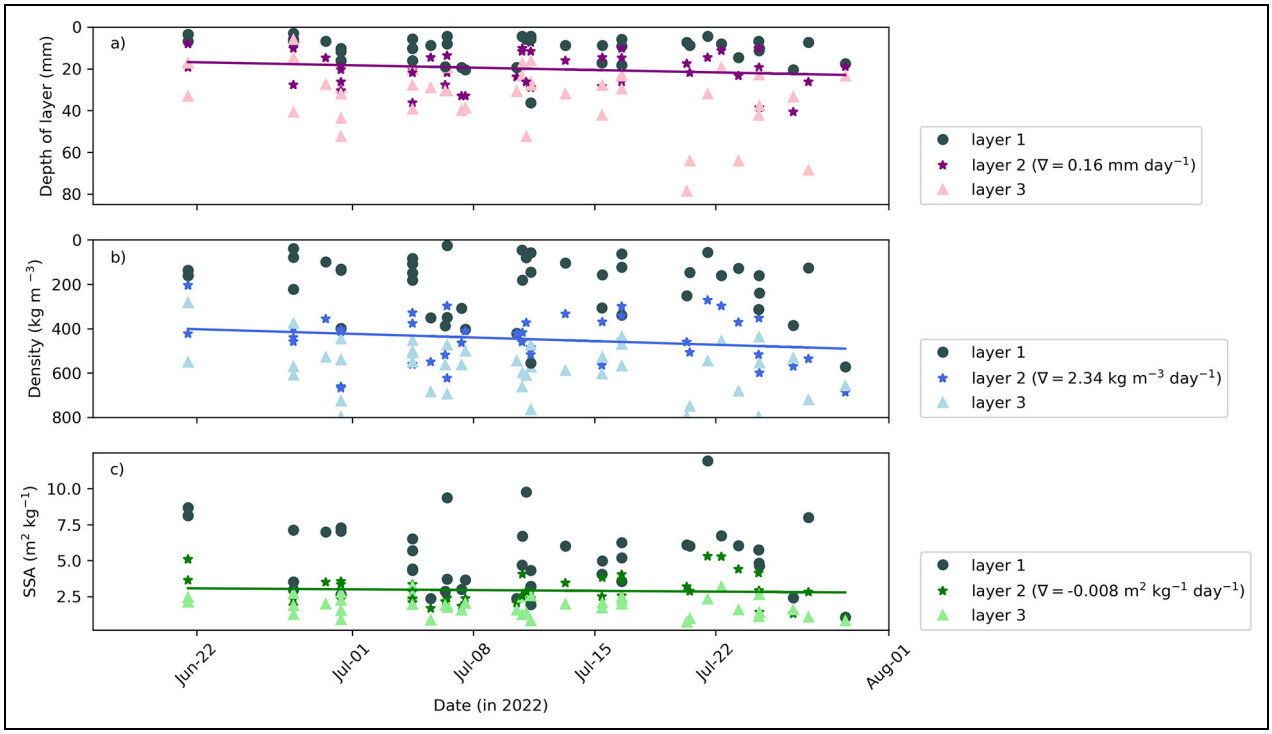

Figure 7. Time series of parameters for surface scattering layer samples. Individual micro-computed tomography samples of the surface scattering layer (SSL) were collected in the field. Once the profiles of density and specific surface area (SSA) were obtained for each sample, the sample profiles were separated into three weighted layers, as described in the methods section. For each layer, (a) depth, (b) density and (c) SSA are plotted against the time the samples were collected. The lines of best fit are given for layer 2 in each panel. Gradients of these best-fit lines are indicated in the inset legends. The surface of melting sea ice is defined as the origin (z = 0). Due to low density and high SSA at the surface of the SSL samples, the y-axis is inverted in (b) to better visualize the properties of the three layers.

with the microCT samples shown in **Figure 8c**, where the images appear to become more pillared over time. The SSA and density profiles shown in **Figure 8b** are almost identical for each sample, implying that simple density and SSA profiles are not documenting the visually changing microstructure seen in **Figure 8c**. **Figure 8d** is discussed at the end of the results section.

The correlation between the microstructure and the reflectivity at 850 nm is visualized in **Figure 9a** and **b**. The relationship between the average SSA (**Figure 9a**) and SSA multiplied by density (**Figure 9b**) of different layers of the microCT sample and the co-located NIR_{850} measurement was plotted. The r^2 value for each layer was calculated to identify the layers of higher interest, i.e., those with the higher r^2 values and the top 0–20 mm with a very low r^2 value.

Figure 10a shows probability density functions (PDFs) of the complete datasets of NIR_{850}, ASD_{850} and $TARTES_{850}$ and for the co-located samples only (**Figure 10b**). The "NIR_{850} All" has a mode of 0.596, comparable to the "ASD_{850} All" mode at 0.597. This close similarity indicates that the NIRbox is a reliable instrument to measure reflectance at 850 nm and can be used to better understand the spatial and temporal variability of sea ice. The "$TARTES_{850}$ All" mode is 0.69, which is the first indication of the overestimation of the RTM model. An Anderson-Darling normality test was conducted to determine if the data samples had a Gaussian distribution. The NIR_{850} and ASD_{850} co-located data samples were Gaussian at the 1–15% level. The $TARTES_{850}$ co-located data samples were Gaussian at the 1–5% level. The range of each dataset is 0.71 for "ASD_{850} All," 0.16 for "NIR_{850} All," and 0.27 for "$TARTES_{850}$ All." The spread of values in the "ASD_{850} All" dataset could be due to a wrongly classified surface (we tried to analyze only ASD measurements indicated as SSL samples, but misclassifications may have been likely) or external influences on the spectral albedo, such as changes in azimuth angle or influence from adjacent surfaces (e.g., neighbouring melt ponds). Working through each ASD measurement and its corresponding overview image would have helped to understand these lower values; however, that objective was not the focus of this study. Our focus here is on the co-located datasets (**Figures 10b** and **11**).

Figure 11 compares all co-located samples of NIR_{850} and ASD_{850} against $TARTES_{850}$. The overestimation of $TARTES_{850}$ values is apparent, with all the points lying below the 1:1 line. The difference in albedo values of the co-located ASD_{850} (mean = 0.58; $\sigma^2 = 0.003$, n = 7), NIR_{850} (mean = 0.60; $\sigma^2 = 0.002$, n = 7) and $TARTES_{850}$ datasets (mean = 0.66; $\sigma^2 = 0.004$, n = 4) was not significant for $ASD_{850}NIR_{850}$ ($t(16) = 0.5$; $p > 0.05$). However, it was significant for NIR_{850} $TARTES_{850}$ ($t(32) = 0.001$; $p < 0.05$) and ASD_{850} $TARTES_{850}$ ($t(24) = 0.003$;

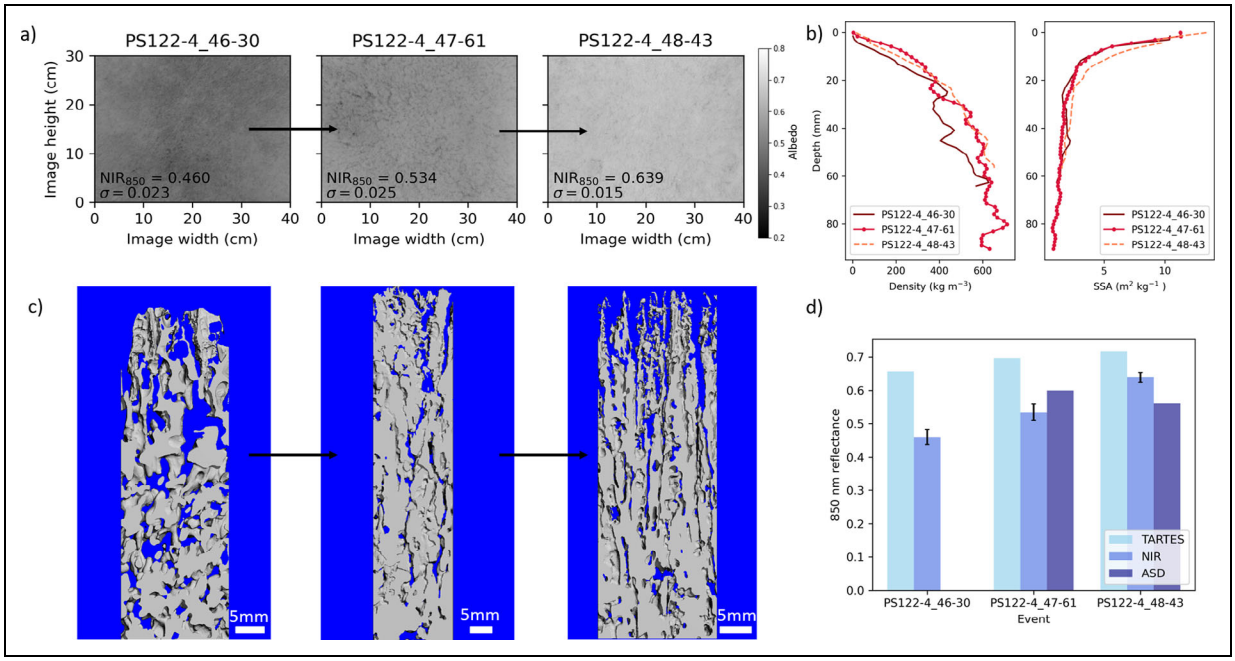

Figure 8. Changes in the microstructure and their influence on the reflectance at 850 nm. This figure is to aid in visualizing the influence of microstructure on the NIR_{850} reflectance at the sampling location designated optics-LDL (see **Figure 5b**). The panels show: (a) the first three NIRbox images (as shown in **Figure 5c**) taken on the 2020 dates (and file names) of July 6 (2020_0706_134819_058.TIFF), July 13 (2020_0713_131206_016.TIFF), and July 21 (2020_0721_140144_094.TIFF); (b) the almost identical co-located density and specific surface area (SSA) profiles of the three microcomputer tomograph (microCT) samples; (c) visualization of the three microCT samples; and (d) comparison of the three types of reflectance measurements, $TARTES_{850}$ from the microCT samples, NIR_{850} from the NIRbox images, and ASD_{850} from the analytical spectral device at 850 nm.

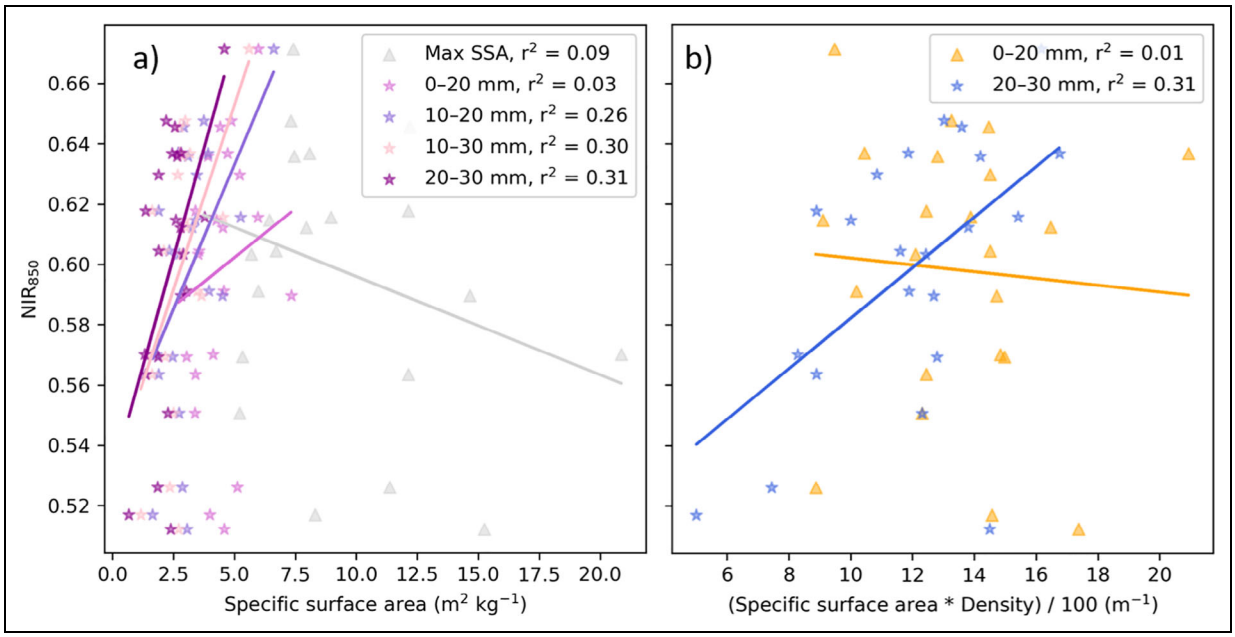

Figure 9. The relationship between specific surface area and reflectance at 850 nm by layer. Having acquired co-located NIRbox images and micro-computed tomography (microCT) samples allowed us to compare the microstructural parameters of the surface scattering layer (SSL) to the reflectance of the SSL at 850 nm. The microCT samples were divided into 10 to 50 mm layers and tested for the highest r^2 value in relation to the corresponding NIR_{850} value; the layers of higher interest are plotted here. In (a), the average specific surface area (SSA) of the layers is plotted against co-located NIR_{850} values, with layer depth and r^2 value provided in the inset legend. The maximum SSA (max SSA) measured for the sample was often at the surface. In (b), the same samples are shown as in (a), but the SSA and density have been multiplied to show the combined relationship of these two parameters with the reflectance at 850 nm.

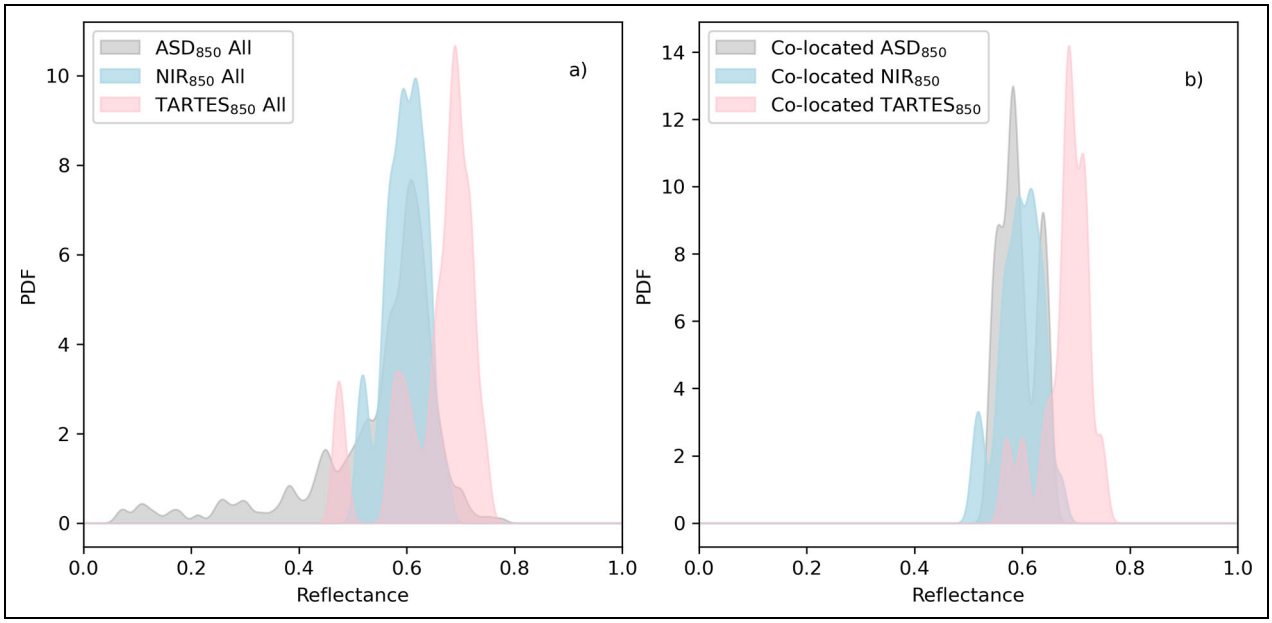

Figure 10. Probability density functions of the three methods used to determine reflectance at 850 nm. This figure compares colour-coded datasets from the three methods used to determine reflectance at 850 nm: near-infrared imaging from the NIRbox (NIR_{850}), data from the analytical spectral device (ASD_{850}), and micro-computed tomography data input to a radiative transfer model ($TARTES_{850}$.). In (a), all measurements throughout July and the beginning of August are shown for ASD_{850}, NIR_{850} and $TARTES_{850}$. In (b), only co-located measurements are shown when the three instruments were deployed simultaneously in the same place.

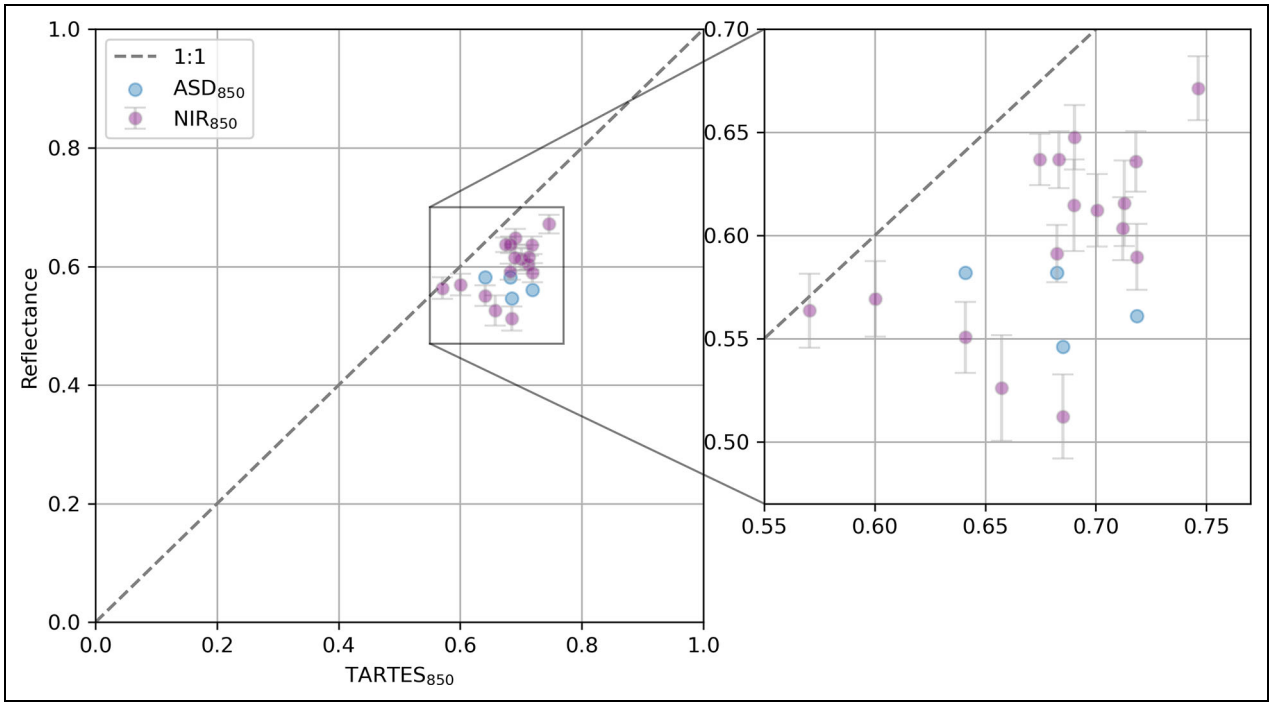

Figure 11. Co-located measurements from the three methods used to determine reflectance at 850 nm. This figure shows the reflectance at 850 nm, calculated from the micro-computed tomography data input to a radiative transfer model ($TARTES_{850}$), compared to measurements of reflectivity by near-infrared imaging from the NIRbox (NIR_{850}) and by the analytical spectral device (ASD_{850}). It uses the same data as the co-located measurements in **Figure 10b**. The NIR_{850} error bars represent one standard deviation of the NIRbox image pixel values. The dark grey line denotes the 1:1 line.

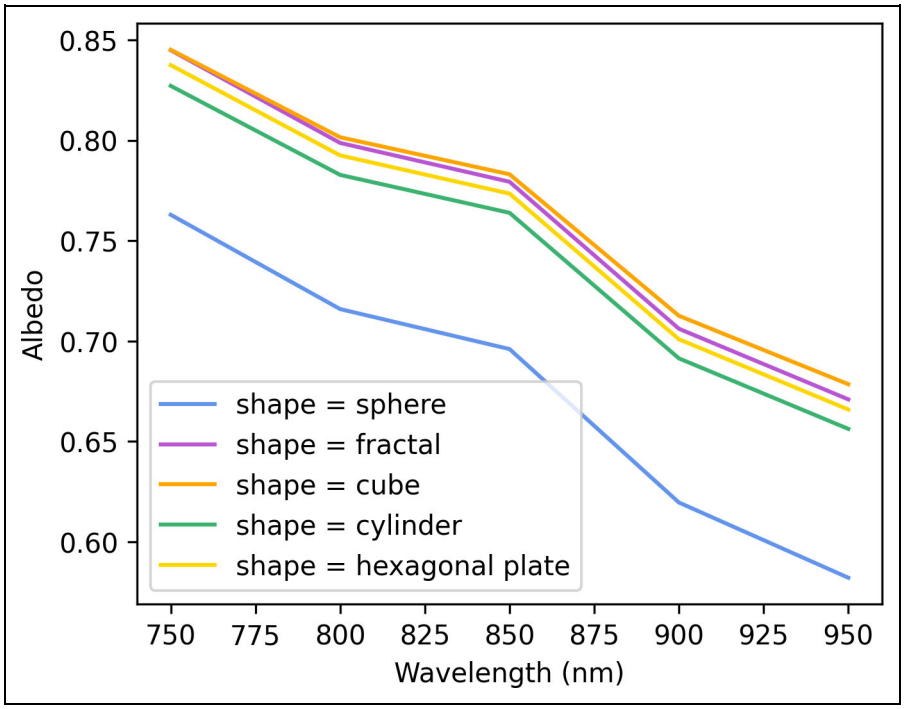

Figure 12. A test of the influence of the asymmetry factor on the modelled output albedo. This figure shows the results of a test of the influence of different asymmetric factors (g) and absorption enhancement parameters (B) on output from the radiative transfer model (TARTES) with data input from micro-computed tomography. The different shapes in the inset legend represent different combinations of g and B. A two-layer surface scattering layer structure and a drained layer were inputs for this test. The density and specific surface area were taken from the average of all profiles in this study (see more information in the methods section). For this study, the 850 nm wavelength is of interest.

$p < 0.05$). σ^2 represents variance, t (16) represents the t-test (assuming unequal variances) value with 16 degrees of freedom, and 0.05 is the significance level. If the p-value is less than the significance level, the hypothesis that the two means of the two datasets are equal can be rejected.

Returning to **Figure 8**, which shows three different visits to one snowpit site. The overestimation of the TARTES/microCT approach with respect to the NIRbox image and the ASD can be seen (**Figure 8d**). The $TARTES_{850}$ values show an increasing trend similar to the NIR_{850} values. However, for the three snowpit site visits, TARTES overestimates by 0.20, 0.16 and 0.08, respectively. The $TARTES_{850}$ value does not lie within one standard deviation of the NIR values (indicated by the black error bars in **Figure 8d**).

The TARTES overestimation is significant, as seen in the p-test values (given above). A test was conducted to understand the influence of changing the asymmetry factor on the TARTES model output. **Figure 12** shows the output of this test at different wavelengths. At 850 nm, the resulting albedo was 0.783 for a cube ($g = 0.77$, $B = 1.56$) and 0.696 for a sphere. Therefore, the results would increase in albedo if a different asymmetry factor was used, indicating that another factor within the model causes the overestimation.

4. Discussion

Previous studies on the reflective properties of the melting sea ice surface did not include the influence of SSL geometry on the albedo due to a lack of measurements. This study is the first to measure the micro- and macro-structure of the SSL and establish the link between the SSL microstructure and reflectance at 850 nm. In the microCT measurements, we observed a coarse and porous structure with a small SSA at the surface that increases with depth. **Figure 6** shows that density was highly variable between all samples and at the surface of the SSA profiles in the top layer, where it ranged between 5 and 10 $m^2\ kg^{-1}$. In the lower layers, the SSA profiles are more consistent between samples. In the surface layer (layer one), SSA was highly variable, with a thickness varying around 10–20 mm. However, due to the low density of layer one, its influence on the optical properties is minimal, as light can penetrate deeper layers.

Unlike wet snow metamorphism, which coarsens with age (Raymond and Tusima, 1979), the SSL did not coarsen, maintaining its density and SSA in the lower layers throughout the melt season. This lack of coarsening and consistency in the density and SSA is due to the different processes. In contrast to coarsening and porosity reduction when snow undergoes melt, the SSL acts in the opposite direction: the porosity increases as it goes from a solid ice structure to a porous SSL. As a result of surface ablation and the DL becoming more porous as it melts preferentially at the grain boundaries, the SSL regenerates and maintains a consistent microstructural profile throughout the melt season. In the time series in **Figure 7**, the gradient of the

density and SSA line of best fit for layer two does not vary temporally over the study period. As mentioned in the introduction, the sea ice extent at the end of summer 2020 was the second lowest in the satellite record (Perovich et al., 2020), and the melt season lasted more than a month longer than usual (Rinke et al., 2021). In this study, we found that the SSL remained constant over time. Therefore, a longer melt season does not influence the SSL microstructure. We can conclude that this study represents the typical optical and microstructural properties of the surface scattering layer in the high Arctic on first and second-year level ice.

Figure 4 shows examples of NIR_{850} from NIRbox images which, when compared against ASD_{850} in **Figure 5**, remained within one standard deviation of the ASD_{850} daily mean. This close correspondence indicates that the new NIRbox measurement technique can accurately measure surface reflectance at 850 nm. This novel method is not influenced by incoming radiation, cloud cover, surface inclination or azimuth angle, which may influence the ASD measurements. Reference images taken prior to each measurement show no influence from external light.

After confirming that the NIRbox is a reliable instrument to assess the albedo of the ice surface at 850 nm, we used the NIR_{850} values to investigate the spatial and temporal variability of the SSL reflectance at 850 nm. **Figure 4** shows the large spatial variability in the month of July. The NIR_{850} values show a minimum of 0.46 and a maximum of 0.675. At this wavelength, the spatial variability in the optical properties could be a result of the microstructure. We are aware that the microstructure of the SSL plays a significant role in the optical properties and reflectance of the surface (Light et al., 2008). In the rest of this study, we tried to understand how the microstructure influences optical properties through investigations of co-located measurements and radiative transfer modelling.

Most locations had little to no change in reflectivity over the period examined. However, one location showed a consistent increase in reflectivity. **Figure 5** shows a time series grouped by location, with the NIRbox images at this specific location (opticsLDL) showing a consistent increase in reflectivity (**Figure 5c**). **Figure 8** provides more measurement detail at opticsLDL: the microstructure is observed to change visually and become more pillared, but the density and SSA profiles remain largely unchanged (**Figure 8c**). These results imply that another optical analysis is needed, not based on the density and SSA of spheres used in TARTES. The microstructure in the third image in **Figure 8c** is likely to have more internal scattering compared to the first two microstructures. In an attempt to understand the influence of the microstructural properties on the reflectance values and to see if a specific depth range influences the overall reflectance, we conducted a layered study on all the co-located samples, visualized in **Figure 9**. The results show a low correlation of the average SSA of the upper layers (0–20 mm) of the microCT sample to the NIR_{850} values and a higher correlation to the lower layers (10–30 mm, with the highest r^2 value of 0.31). They imply that lower layers affect overall reflectance more than surface layers, but the low r^2 values of all trends in **Figure 9** mean that all layers have an important effect. The low density and pillared structure combined with an r^2 value of 0.09 at the surface indicates that the underlying layer of the SSL below 20 mm is more relevant for the reflectance.

Aware that the microstructure is influencing the reflectance at 850 nm, we then assessed directly, by introducing an RTM (TARTES), how the models represent these changes in microstructure and the influence on the optical properties. By comparing the three measurement approaches, we searched for any discrepancies between them. The probability density functions in **Figure 10** introduce TARTES and compare the reflectance of the SSL on level ice for NIR_{850}, ASD_{850} and $TARTES_{850}$. **Figure 10a** compares the reflectance for all measurements on Leg 4. **Figure 10b** shows the co-located measurements, representing the same dataset as **Figure 11**. The comparable mean values of the NIR_{850} and ASD_{850} are another indication that the NIRbox is a reliable instrument to assess the albedo of the ice surface at 850 nm. We conclude that the NIRbox is an excellent way to get information that can be used to determine the SSA of the SSL. However, the t-test results show significant differences in the mean of the $TARTES_{850}$ dataset compared to ASD_{850} and NIR_{850}. We find that using the microstructure (density, SSA and layer thickness) as an input into the TARTES RTM produces a 10–15% overestimation of the reflectance at 850 nm. This overestimation was not due to the asymmetry factor, as tested in **Figure 11**, as changing this factor increased the output and did not explain the overestimation. Alternative reasons for the overestimation could be:

a) The footprints differ between the three measurement techniques (microCT $= 5.03 \times 10^{-3}$ m^2, ASD approximately 1.77 m^2, and NIRbox $= 0.12$ m^2). The NIRbox and the ASD include more spatial variability in the measurements. As seen in **Figure 4**, there are darker patches that increase the standard deviation of the NIR_{850} pixel values. The microCT sample size may be too small to capture the meter scale spatial variability, and these darker patches would not be sampled. However, this scaling problem would not influence all co-located measurement points, as many NIR_{850} images did not include the dark patches seen in **Figure 4**. The different footprints between techniques are thus likely to explain a few of the underestimated values but not the general underestimation of the TARTES model.
b) In TARTES, we are averaging the extremely intricate and complex aspects of microstructure. The NIR_{850} image and the microCT-image clearly show vertical air gaps with a width of many wavelengths and depth of several millimeters to centimeters (**Figure 3**). Such a geometry resembles a scaled-down vegetation canopy structure (Shabanov and Gastellu-Etchegorry, 2018). The low density and pillared structure at the surface before averaging into layers means that the underlying layer two is more relevant for the reflectance. However, when

we average this structure into layers, we increase the density, decrease the SSA at the very surface in layer one and produce an artificial grain size in a homogeneous layer. This averaging may thus result in an overestimation of the reflectance as less radiation penetrates to the lower depths of the SSL, compared to a pillared structure with a low density at the surface and vertical air gaps. We suggest that this structure is too complex to average into layers. An RTM assuming horizontally homogeneous layers, as used in this study, cannot account for the pillared microstructure and is not appropriate for this type of structure. This microstructure complexity is also visible in **Figure 8**, where the microstructure changes visibly, but the density and SSA profiles remain the same, indicating that a different analysis is needed. Future work could benefit from using either a ray tracing approach, instead of explicitly solving the RT equation, or a more appropriate RTM, possibly based on a stochastic Beer-Lambert-Bouguer law commonly used for vegetation canopy structures (as represented in figure 3 of Shabanov and Gastellu-Etchegorry, 2018) to better represent the intricate structures on melting sea ice.

The physical and optical properties of the melting sea ice surface are influenced by preferential melt at the grain boundaries. We observed a large spatial variability in the microstructure of the sea ice surface, with different surface types both in the field and in our measurements. The SSL is just one of many categories of surface structures appearing on melting sea ice. We found that spatial variability of the microstructure of the sea ice surface is high when ice has different histories or freezing processes, which leads to an array of surface melt patterns and structures caused by the ice having different grain boundaries. These different surface types provide an extensive range of reflectance values. In previous studies, the surface of sea ice was categorized as ponded or bare ice/SSL. We support the idea that the spatial variability of sea ice needs to be incorporated when modelling the microstructure and reflectance of the sea ice surface. We propose that ice surface history, expressed in the macrostructure, is a key parameter to understanding the microstructural spatial variability of the ice. However, macrostructure was not the focus of this study, and we used only level ice with no previous ridging, ponding or freezing history that would have created different grain boundaries. We focused on level ice with a homogeneous SSL. A future study, beyond the scope of this one, could profitably investigate the influence of freeboard on microstructure and reflectance.

5. Conclusion

For the first time, this paper shows measurements of the SSL microstructure and its relation to optical properties in the near-infrared wavelength of 850 nm. By co-locating microstructural measurements with reflectance measurements, we could better understand the SSL temporal and spatial variability. The findings are as follows:

1. The average SSL profile consisted of a vertical pillared structure with a high average SSA of 4.08 $\pm$ 1.18 $m^2\ kg^{-1}$ (σ) and a low density of 332 $\pm$ 84 kg m^{-3} (σ) at the surface. We observed consistent patterns in the microstructure profile across spatial and temporal sampling. Most of the variability was focused in the top 0–20 mm (**Figure 2**). This variability in the microstructure introduced spatial variability in the optical properties of the melting sea ice.
2. Unlike snow, where wet snow metamorphism causes a coarsening of grains and albedo decreases with age, the SSL regenerated and maintained its microstructure over the season. The SSL low density and pillared structure observed at the surface mean that the underlying layer below 20 mm is more relevant for reflectance. The microstructure below 20 mm was consistent through the melt season, and, at most locations, no temporal variability was observed in the optical properties of the SSL. We obtained a distribution of melting sea ice reflectance and concluded that temporal evolution was small. We do not have a multimodal distribution (in **Figure 10**) that would have resulted from different ice ages or changes in the freeboard. The influence of these parameters was smaller than the standard deviation of all samples and within the limits of the observed distribution. The melt rate may have varied, but the SSL always regenerated in the same manner. Future large-scale changes in the surface reflectance of the sea ice cannot be ascribed to a changing SSL. Therefore, future work could benefit from a focus on the melt pond fraction, ridges and changes in melt pond optical properties.
3. The new NIRbox method was shown to be a low-cost, easy-to-use method for measuring reflectance at wavelengths sensitive to snow and SSL microstructure. In this study, the NIRbox was used to measure the surface reflectance at 850 nm without any influence from incoming radiation (as shown through the reference images taken at each event), cloud cover, surface inclination or azimuth angle. The NIRbox contributes considerable knowledge to research on the surface reflectance of sea ice and can be used to answer critical questions on the variability of albedo.
4. For the first time, we calculated albedo using microCT-derived SSA, thickness, and density in the TARTES model. We observed a 10–15% overestimation when using this approach. Reasons for the overestimation could include: a) insufficient sample size to represent the microstructure, as spatial variability at the meter scale is important for the two in situ optical measurements, or b) insufficient model representation in TARTES (which uses the Mie solution to Maxwell's equation). TARTES does not consider anisotropy and estimates the structure as spheres in discrete layers. We calculated geometrical anisotropy for the samples, but this parameter is not useful when calculating optical properties. Full

structural anisotropy and star volume would be interesting geometrical measures to make in a future study. Future work could benefit from using either a ray tracing approach instead of explicitly solving the RT equation or a more appropriate RTM. This RTM could be based on a stochastic Beer-Lambert-Bouguer law, which considers anisotropy and is commonly used for vegetation canopy structures (as represented in figure 3 in Shabanov and Gastellu-Etchegorry, 2018), to better represent the intricate structures on melting sea ice.

Data accessibility statement

All data used in this article are publicly available on the MOSAiC archives in PANGAEA (https://www.pangaea.de/) and the National Science Foundation Arctic Data Center (http://arcticdata.io) (Macfarlane et al., 2021; Smith et al., 2021; Macfarlane et al., 2022a; Macfarlane et al., 2022b). Snowpit raw data can be found at https://doi.org/10.1594/PANGAEA.935934 (Macfarlane et al., 2021); snowpit near-infrared (NIR) images can be found at https://doi.org/10.1594/PANGAEA.940129 (Macfarlane et al., 2022a); snowpit microCT dataset can be found at PANGAEA, PDI-32502 (Macfarlane et al., 2022b); snowpit overview photos can be found at https://doi.org/10.1594/PANGAEA.940056 (Macfarlane et al., 2022c); and snowpit isotope data can be found at PANGAEA, PDI-32381 (Macfarlane et al., 2022d). ASD data and the corresponding photos have been archived at http://doi.org/10.18739/A2FT8DK8Z and http://doi.org/10.18739/A2B27PS3N (Smith et al., 2021).

Supplemental files

The supplemental files for this article can be found as follows:

Figure S1. Figure S2. Docx

Acknowledgments

Datasets used in this article were produced as part of the international Multidisciplinary drifting Observatory for the Study of the Arctic Climate (MOSAiC) with the tag MOSAiC20192020 and the Project_ID: AWI_PS122_00. We thank all people involved in the expedition of the Research Vessel *Polarstern* (Knust, 2017) during MOSAiC in 2019–2020 as listed in Nixdorf et al. (2021). We would like to thank Scanco Medical AG for lending and supporting the use of the MicroCT90 throughout the MOSAiC expedition. We also thank the anonymous reviewer and Chris Polashenski for their time and effort spent in reviewing the article. We appreciate their valuable feedback, which greatly improved the clarity of this study.

Funding

Swiss Polar Institute (SPI reference DIRCR-2018-003) Funder ID http://dx.doi.org/10.13039/501100015594.

European Union's Horizon 2020 research and innovation program projects ARICE (grant 730965) for berth fees associated with the participation of the DEARice project.

WSL Institute for Snow and Avalanche Research SLF. WSL_201812N1678. Funder ID: http://dx.doi.org/10.13039/501100015742.

MW conducted this work under the National Aeronautics and Space Administration's New Investigator Program in Earth Science (80NSSC20K0658).

MMS was supported by NSF OPP-1724467 and OPP-1724748 and OPP-2138787.

FL was supported by the German Federal Ministry for Economic Affairs and Energy (BMWi) project ArcticSense (50EE1917A).

Competing interests

The authors declare that they have no known competing interests.

Author contributions

Conceptualization, methodology, formal analysis, data curation, investigation, writing (original draft, review and editing), and visualization: ARM.

Conceptualization, methodology, investigation, writing (review and editing): RD.

Writing (review and editing): MMS, BL, MN, HHR, MW, FL.

Instrument provider, writing (review and editing): SH.

Project administration, funding acquisition, conceptualization, methodology, investigation, writing (review and editing): MS.

References

Britannica, T. Editors of Encyclopaedia. 2014. *firn. Encyclopedia Britannica*. Available at https://www.britannica.com/science/firn. Accessed March 28, 2023.

Cole, DM, **Shapiro, LH.** 1998. Observations of brine drainage networks and microstructure of first-year sea ice. *Journal of Geophysical Research: Oceans* **103**(C10): 21739–21750. DOI: http://dx.doi.org/10.1029/98JC01264.

Colman, RA. 2013. Surface albedo feedbacks from climate variability and change. *Journal of Geophysical Research: Atmosphere* **118**: 2827–2834.

Dadic, R, **Mullen, PC**, **Schneebeli, M**, **Brandt, RE**, **Warren, SG.** 2013. Effects of bubbles, cracks, and volcanic tephra on the spectral albedo of bare ice near the Transantarctic Mountains: Implications for sea glaciers on Snowball Earth. *Journal of Geophysical Research: Earth Surface* **118**(3): 1658–1676.

Dash, JG, **Rempel, AW**, **Wettlaufer, JS.** 2006. The physics of premelted ice and its geophysical consequences. *Reviews of Modern Physics* **78**(3): 695.

Ding, Q, **Schweiger, A**, **L'Heureux, M**, **Battisti, DS**, **Po-Chedley, S**, **Johnson, NC**, **Blanchard-Wrigglesworth, E**, **Harnos, K**, **Zhang, Q**, **Eastman, R**, **Steig, EJ.** 2017. Influence of high-latitude atmospheric circulation changes on summertime Arctic sea ice. *Nature Climate Change* **7**(4): 289–295.

Dozier, J. 1992. Remote sensing of alpine snow cover in visible and near-infrared wavelengths, in Kaitowski, M, Decker, MK eds., *Proceedings from a symposium: Snow science: Reflections on the past, perspectives on*

the future. Alta, UT: The Center for Snow Science at Alta: 10–21.

Ehn, JK, **Papakyriakou, TN**, **Barber, DG.** 2008. Inference of optical properties from radiation profiles within melting landfast sea ice. *Journal of Geophysical Research: Oceans* **113**(C9): C09024. DOI: https://doi.org/10.1029/2007JC004656.

Eicken, H. 2003. From the microscopic, to the macroscopic, to the regional scale: Growth, microstructure and properties of sea ice, in Thomas, DN, Dieckmann, GS eds., *Sea ice: An introduction to its physics, chemistry, biology and geology*. New York, NY: Wiley: 22–81.

Flanner, MG, **Shell, KM**, **Barlage, M**, **Perovich, DK**, **Tschudi, MA.** 2011. Radiative forcing and albedo feedback from the Northern Hemisphere cryosphere between 1979 and 2008. *Nature Geoscience* **4**: 151–155.

Frantz, CM, **Light, B**, **Farley, SM**, **Carpenter, S**, **Lieblappen, R**, **Courville, Z**, **Orellana, MV**, **Junge, K.** 2019. Physical and optical characteristics of heavily melted "rotten" Arctic sea ice. *The Cryosphere* **13**(3): 775–793.

Freitag, J, **Eicken, H.** 2003. Meltwater circulation and permeability of Arctic summer sea ice derived from hydrological field experiments. *Journal of Glaciology* **49**(166): 349–358.

Gergely, M, **Wolfsperger, F**, **Schneebeli, M.** 2014. Simulation and validation of the InfraSnow: An instrument to measure snow optically equivalent grain size. *IEEE Transactions on Geoscience and Remote Sensing* **52**(7): 4236–4247. https://dx.doi.org/10.1109/TGRS.2013.2280502.

Grenfell, TC. 1991. A radiative transfer model for sea ice with vertical structure variations. *Journal of Geophysical Research: Oceans* **96**(C9): 16991–17001.

Grenfell, TC, **Light, B**, **Perovich, DK.** 2006. Spectral transmission and implications for the partitioning of shortwave radiation in arctic sea ice. *Annals of Glaciology* **44**: 1–6. DOI: http://dx.doi.org/10.3189/172756406781811763.

Grenfell, TC, **Maykut, GA.** 1977. The optical properties of ice and snow in the Arctic Basin. *Journal of Glaciology* **18**(80): 445–463.

Grenfell, TC, **Perovich, DK**. 1981. Radiation absorption coefficients of polycrystalline ice from 400–1400 nm. *Journal of Geophysical Research: Oceans* **86**(C8): 7447–7450.

Hildebrand, T, **Rüegsegger, P.** 1997. A new method for the model-independent assessment of thickness in three-dimensional images. *Journal of Microscopy* **185**(1): 67–75. DOI: http://dx.doi.org/10.1046/j.1365-2818.1997.1340694.x.

Huang, W, **Lei, R**, **Han, H**, **Li, Z.** 2016. Physical structures and interior melt of the central Arctic sea ice/snow in summer 2012. *Cold Regions Science Technology* **124**(1): 127–137. DOI: http://dx.doi.org/10.1016/j.coldregions.2016.01.005.

Joseph, J, **Wiscombe, W**, **Weinman, J.** 1977. The Delta-Eddington approximation for radiative flux transfer. *Journal of Atmospheric Sciences* **33**(12): 2452–2459.

Knust, R. 2017. Polar research and supply vessel POLARSTERN operated by the Alfred-Wegener-Institute. *Journal of Large-Scale Research Facilities JLSRF* **3**: A119. DOI: http://dx.doi.org/10.17815/jlsrf-3-163.

Krumpen, T, **von Albedyll, L**, **Goessling, HF**, **Hendricks, S**, **Juhls, B**, **Spreen, G**, **Willmes, S**, **Belter, HJ**, **Dethloff, K**, **Haas, C**, **Kaleschke, L**, **Katlein, C**, **Tian-Kunze, X**, **Ricker, R**, **Rostosky, P**, **Rückert, J**, **Singha, S**, **Sokolova, J.** 2021. MOSAiC drift expedition from October 2019 to July 2020: Sea ice conditions from space and comparison with previous years. *The Cryosphere* **15**: 3897–3920. DOI: http://dx.doi.org/10.5194/tc-15-3897-2021.

Leroux, C, **Lenoble, J**, **Brogniez, G**, **Hovenier, JW**, **De Haan, JF.** 1999. A model for the bidirectional polarized reflectance of snow. *Journal of Quantitative Spectroscopy and Radiative Transfer* **61**(3): 273–285.

Libois, Q, **Picard, G**, **Dumont, M**, **Arnaud, L**, **Sergent, C**, **Pougatch, E**, **Vial, D.** 2014. Experimental determination of the absorption enhancement parameter of snow. *Journal of Glaciology* **60**(222): 714. DOI: http://dx.doi.org/10.3189/2014JoG14J015.

Libois, Q, **Picard, G**, **France, J**, **Arnaud, L**, **Dumont, M**, **Carmagnola, C**, **King, MD.** 2013. Influence of grain shape on light penetration in snow. *The Cryosphere* **7**: 1803–1818. DOI: http://dx.doi.org/10.5194/tc-7-1803-2013.

Light, B, **Grenfell, TC**, **Perovich, DK.** 2008. Transmission and absorption of solar radiation by Arctic sea ice during the melt season. *Journal of Geophysical Research: Oceans* **113**(3). DOI: http://dx.doi.org/10.1029/2006JC003977.

Light, B, **Holland, M**, **Smith, M**, **Perovich, D**, **Webster, M**, **Clemens-Sewell, D**, **Linhardt, F**, **Raphael, I**, **Bailey, D.** 2021. The MOSAiC sea ice albedo record: Its context and role for informing improved surface radiative budgets in a climate model, in *EGU General Assembly Conference Abstracts*. EGU21–8585. DOI: http://dx.doi.org/10.5194/egusphere-egu21-8585. Accessed March 28, 2023.

Light, B, **Perovich, DK**, **Webster, MA**, **Polashenski, C**, **Dadic, R.** 2015. Optical properties of melting first-year Arctic sea ice. *Journal of Geophysical Research: Oceans* **120**(11): 7657–7675. DOI: http://dx.doi.org/10.1002/2015JC011163.

Light, B, **Smith, MM**, **Perovich, DK**, **Webster, M**, **Holland, M**, **Linhardt, F**, **Raphael, IA**, **Clemens-Sewall, D**, **MacFarlane, A**, **Anhaus, P**, **Bailey, D.** 2022. Arctic sea ice albedo: Spectral composition, spatial heterogeneity, and temporal evolution observed during the MOSAiC drift. *Elementa: Science of the Anthropocene* **10**(1): 000103.

Lombardo, M, **Schneebeli, M**, **Löwe, H.** 2021. A casting method using contrast-enhanced diethylphthalate for micro-computed tomography of snow. *Journal of Glaciology* **67**(265): 847–861. DOI: http://dx.doi.org/10.1017/jog.2021.35.

Macfarlane, AR, **Schneebeli, M**, **Dadic, R**, **Wagner, DN**, **Arndt, S**, **Clemens-Sewall, D**, **Hämmerle, S**, **Hannula, H-R**, **Jaggi, M**, **Kolabutin, N**, **Krampe, D**,

Lehning, M, **Matero, I**, **Nicolaus, M**, **Oggier, M**, **Pirazzini, R**, **Polashenski, C**, **Raphael, I**, **Regnery, J**, **Shimanchuck, E**, **Smith, MM**, **Tavri, A.** 2021. Snowpit raw data collected during the MOSAiC expedition [dataset]. *PANGAEA*. DOI: http://dx.doi.org/10.1594/PANGAEA.935934.

Macfarlane, AR, **Schneebeli, M**, **Dadic, R**, **Wagner, DN**, **Arndt, S**, **Clemens-Sewall, D**, **Hämmerle, S**, **Hannula, H-R**, **Jaggi, M**, **Kolabutin, N**, **Krampe, D**, **Lehning, M**, **Matero, I**, **Nicolaus, M**, **Oggier, M**, **Pirazzini, R**, **Polashenski, C**, **Raphael, I**, **Regnery, J**, **Shimanchuck, E**, **Smith, MM**, **Tavri, A.** 2022a. Snowpit near-infrared (NIR) images collected during the MOSAiC expedition [dataset]. *PANGAEA*. DOI: http://dx.doi.org/10.1594/PANGAEA.940129.

Macfarlane, AR, **Schneebeli, M**, **Dadic, R**, **Wagner, DN**, **Arndt, S**, **Clemens-Sewall, D**, **Hämmerle, S**, **Hannula, H-R**, **Jaggi, M**, **Kolabutin, N**, **Krampe, D**, **Lehning, M**, **Matero, I**, **Nicolaus, M**, **Oggier, M**, **Pirazzini, R**, **Polashenski, C**, **Raphael, I**, **Regnery, J**, **Shimanchuck, E**, **Smith, MM**, **Tavri, A.** 2022b. Snowpit MicroCT profiles during the MOSAiC expedition [dataset]. *PANGAEA*. PDI-32502. DOI: https://doi.org/10.1594/PANGAEA.952794.

Macfarlane, AR, **Schneebeli, M**, **Dadic, R**, **Wagner, DN**, **Arndt, S**, **Clemens-Sewall, D**, **Hämmerle, S**, **Hannula, H-R**, **Jaggi, M**, **Kolabutin, N**, **Krampe, D**, **Lehning, M**, **Matero, I**, **Nicolaus, M**, **Oggier, M**, **Pirazzini, R**, **Polashenski, C**, **Raphael, I**, **Regnery, J**, **Shimanchuck, E**, **Smith, MM**, **Tavri, A.** 2022c. Snowpit overview photos collected during the MOSAiC expedition [dataset]. *PANGAEA*. DOI: http://dx.doi.org/10.1594/PANGAEA.940056.

Macfarlane, AR, **Schneebeli, M**, **Dadic, R**, **Wagner, DN**, **Arndt, S**, **Clemens-Sewall, D**, **Hämmerle, S**, **Hannula, H-R**, **Jaggi, M**, **Kolabutin, N**, **Krampe, D**, **Lehning, M**, **Matero, I**, **Nicolaus, M**, **Oggier, M**, **Pirazzini, R**, **Polashenski, C**, **Raphael, I**, **Regnery, J**, **Shimanchuck, E**, **Smith, MM**, **Tavri, A.** 2022d. Snowpit stable isotope profiles during the MOSAiC expedition [dataset]. *PANGAEA*. DOI: https://doi.org/10.1594/PANGAEA.952556.

Malinka, A, **Zege, E**, **Heygster, G**, **Istomina, L.** 2016. Reflective properties of white sea ice and snow. *Cryosphere* **10**(6): 2541–2557. DOI: http://dx.doi.org/10.5194/tc-10-2541-2016.

Matzl, M, **Schneebeli, M.** 2006. Measuring specific surface area of snow by near-infrared photography. *Journal of Glaciology* **52**(179): 558–564.

Maykut, GA, **Untersteiner, N.** 1971. Some results from a time-dependent thermodynamic model of sea ice. *Journal of Geophysical Research* **76**(6): 1550–1575.

Meehl, GA, **Chung, CT**, **Arblaster, JM**, **Holland, MM**, **Bitz, CM.** 2018. Tropical decadal variability and the rate of Arctic sea ice decrease. *Geophysical Research Letters* **45**(20): 11–326.

Meier, WN, **Perovich, D**, **Farrell, S**, **Haas, C**, **Hendricks, S**, **Petty, AA**, **Webster, M**, **Divine, D**, **Gerland, S**, **Kaleschke, L**, **Ricker, R**, **Steer, A**, **Tian-Kunze, X**, **Tschudi, M**, **Wood, K.** 2021. Arctic report card: Update for 2021, sea ice. *NOAA Arctic Program*. DOI: http://dx.doi.org/10.25923/y2wd-fn85.

Moritz, RE, **Light, B.** 2014. *Observing and modelling the surface scattering layer of first-year Arctic sea ice*. Washington University of Seattle, Applied Physics Laboratory: 1–7.

Mushtaq, R. 2011. Augmented Dickey Fuller Test. *SSRN*. DOI: http://dx.doi.org/10.2139/ssrn.1911068.

Muskett, RR. 2012. Remote sensing, model-derived and ground measurements of snow water equivalent and snow density in Alaska. *International Journal of Geosciences* **3**: 1127–1136. DOI: http://dx.doi.org/10.4236/ijg.2012.35114.

Nicolaus, M, **Perovich, DK**, **Spreen, G**, **Granskog, MA**, **von Albedyll, L**, **Anhaus, P**, **Angelopoulos, M**, **Arndt, A**, **Belter, HJ**, **Bessonov, V**, **Birnbaum, G**, **Brauchle, JB**, **Calmer, R**, **Cardellach, E**, **Cheng, B**, **Clemens-Sewall, D**, **Dadic, R**, **Damm, E**, **de Boer, G**, **Demir, O**, **Divine, D**, **Fong, A**, **Fons, S**, **Fuchs, N**, **Gabarró, C**, **Gerland, S**, **Gradinger, R**, **Goessling, HF**, **Haapala, J**, **Haas, C**, **Hamilton, J**, **Hannula, H-R**, **Hendricks, S**, **Herber, A**, **Heuzé, C**, **Hoppmann, M**, **Høyland, KV**, **Huntemann, M**, **Hutchings, JK**, **Hwang, B**, **Itkin, P**, **Jaggi, M**, **Jutila, A**, **Kaleschke, L**, **Katlein, C**, **Kolabutin, N**, **Krampe, D**, **Kristensen, SS**, **Krumpen, T**, **Kurtz, N**, **Lampert, A**, **Lange, BA**, **Lei, R**, **Light, B**, **Linhardt, F**, **Liston, G**, **Loose, B**, **Macfarlane, AR**, **Mahmud, M**, **Matero, IO**, **Maus, S**, **Morgenstern, A**, **Naderpour, R**, **Nandan, V**, **Niubom, A**, **Oggier, M**, **Oppelt, N**, **Pätzold, F**, **Petrovsky, T**, **Pirazzini, R**, **Polashenski, C**, **Rabe, B**, **Raphael, IA**, **Regnery, J**, **Rex, M**, **Ricker, R**, **Riemann-Campe, K**, **Rinke, A**, **Rohde, J**, **Salganik, E**, **Scharien, RK**, **Schiller, M**, **Schneebeli, M**, **Semmling, M**, **Sheikin, I**, **Shimanchuk, E**, **Shupe, MD**, **Smith, MM**, **Smolyanitsky, V**, **Sokolov, V**, **Sokolova, J**, **Stanton, TP**, **Stroeve, J**, **Tavri, A**, **Thielke, L**, **Timofeeva, A**, **Tonboe, RT**, **Tsamados, M**, **Wagner, DN**, **Watkins, D**, **Webster, M**, **Wendisch, M.** 2022. Overview of the MOSAiC expedition: Snow and sea ice. *Elementa: Science of the Anthropocene* **10**(1). DOI: http://dx.doi.org/10.1525/elementa.2021.000046.

Nixdorf, U, **Dethloff, K**, **Rex, M**, **Shupe, M**, **Sommerfeld, A**, **Perovich, DK**, **Nicolaus, M**, **Heuzé, C**, **Rabe, B**, **Loose, B**, **Damm, E.** 2021. MOSAiC extended acknowledgement. *Zenodo*. DOI: https://doi.org/10.5281/zenodo.5541624.

Oggier, M, **Eicken, H.** 2022. Seasonal evolution of granular and columnar sea ice pore microstructure and pore network connectivity. *Journal of Glaciology* **68**(271): 833–848.

Perovich, DK. 2002. Seasonal evolution of the albedo of multi-year Arctic sea ice. *Journal of Geophysical Research: Oceans* **107**(C10): SHE–20.

Perovich, DK. 2017. Sea ice and sunlight, in Thomas, DN ed., *Sea ice*. Hoboken, NJ: Wiley Online Library: 110–137.

Perovich, DK, **Meier, W**, **Tschudi, M**, **Hendricks, S**, **Petty, AA**, **Divine, D**, **Farrell, S**, **Gerland, S**, **Haas, C**, **Kaleschke, L**, **Pavlova, O.** 2020. *Arctic report card 2020: Sea ice*. Washington, DC: NOAA.

Perovich, DK, **Polashenski, C.** 2012. Albedo evolution of seasonal Arctic sea ice. *Geophysical Research Letters* **39**(8): L08501. DOI: https://doi.org/10.1029/2012GL051432.

Petrich, C, **Eicken, H.** 2010. Growth, structure and properties of sea ice, in Thomas, DN, Dieckmann, GS eds., *Sea ice. 2nd ed*. Hoboken, NJ: Wiley Online Library: 23–77.

Petrich, C, **Eicken, H.** 2017. Overview of sea ice growth and properties, in Thomas, DN ed., *Sea ice*. Hoboken, NJ: Wiley Online Library: 1–41.

Poürtner, HO, **Roberts, DC**, **Masson-Delmotte, V**, **Zhai, P**, **Tignor, M**, **Poloczanska, E**, **Mintenbeck, K**, **Alegría, A**, **Nicolai, M, Okem, A**, **Petzold, J**, **Rama, B**, **Weyer, NM.** 2019. *IPCC special report on the ocean and cryosphere in a changing climate* (vol. 755). Cambridge, UK: Cambridge University Press: 213. DOI: http://dx.doi.org/10.1017/9781009157964.

Raymond, CF, **Tusima, K.** 1979. Grain coarsening of water-saturated snow. *Journal of Glaciology* **22**(86): 83–105. DOI: http://dx.doi.org/10.3189/S0022143000014076.

Rinke, A, **Cassano, JJ**, **Cassano, EN**, **Jaiser, R**, **Handorf, D.** 2021. Meteorological conditions during the MOSAiC expedition: Normal or anomalous? *Elementa: Science of the Anthropocene* **9**(1). DOI: http://dx.doi.org/10.1525/elementa.2021.00023.

Scanco [internet]. 2019. *MicroCT systems and software*. Available at https://rihof.org/wp-content/uploads/2019/11/microCt-Brochure.pdf. Accessed May 11, 2022. Contact: info@scanco.ch.

Serreze, MC, **Crawford, AD**, **Stroeve, JC**, **Barrett, AP**, **Woodgate, RA.** 2016. Variability, trends, and predictability of seasonal sea ice retreat and advance in the Chukchi Sea. *Journal of Geophysical Research: Oceans* **121**(10): 7308–7325.

Shabanov, N, **Gastellu-Etchegorry, JP.** 2018. The stochastic Beer–Lambert–Bouguer law for discontinuous vegetation canopies. *Journal of Quantitative Spectroscopy and Radiative Transfer* **214**: 18–32. DOI: http://dx.doi.org/10.1016/j.jqsrt.2018.04.021.

Smith, M, **Light, B**, **Perovich, D**, **Webster, M**, **Anhaus, P**, **Clemens-Sewall, D**, **Linhardt, F**, **Macfarlane, A**, **Raphael, I**, **Bozzato, D**, **Brasseur, Z**, **Dadic, R**, **Fons, S**, **Immerz, A**, **Hannula, H-R**, **Hutchings, J**, **Pätzold, F**, **Regnery, J**, **Pirazzini, R**, **Tavri, A.** 2021. Spectral albedo measurements of the sea ice surface during the Multidisciplinary drifting Observatory for the Study of Arctic Climate (MOSAiC) campaign in the Central Arctic Ocean, April–September 2020. Arctic Data Center. DOI: http://dx.doi.org/10.18739/A2FT8DK8Z.

Smith, MM, **Light, B**, **Macfarlane, AR**, **Perovich, DK**, **Holland, MM**, **Shupe, MD.** 2022. Sensitivity of the Arctic sea ice cover to the summer surface scattering layer. *Geophysical Research Letters* **49**(9): e2022GL098349.

Su, W, **Corbett, J**, **Eitzen, Z**, **Liang, L.** 2015. Next-generation angular distribution models for top-of-atmosphere radiative flux calculation from CERES instruments: Validation. *Atmospheric Measurement Techniques* **8**(8): 3297–3313.

Thackeray, CW, **Hall, A.** 2019. An emergent constraint on future Arctic sea-ice albedo feedback. *Nature Climate Change* **9**: 972–978. DOI: http://dx.doi.org/10.1038/s41558-019-0619-1.

Untersteiner, N. 1961. On the mass and heat budget of Arctic sea ice. *Archiv für Meteorologie, Geophysik und Bioklimatologie Serie A* **12**(2): 151–182.

Winton, M. 2006. Surface albedo feedback estimates for the AR4 climate models. *Journal of Climate* **19**(3): 359–365.

Wiscombe, WJ, **Warren, SG.** 1980. A model for the spectral albedo of snow. I: Pure snow. *Journal of Atmospheric Sciences* **37**(12): 2712–2733.

How to cite this article: Macfarlane, AR, Dadic, R, Smith, MM, Light, B, Nicolaus, M, Henna-Reetta, H, Webster, M, Linhardt, F, Hämmerle, S, Schneebeli, M. 2023. Evolution of the microstructure and reflectance of the surface scattering layer on melting, level Arctic sea ice. *Elementa: Science of the Anthropocene* 11(1). DOI: https://doi.org/10.1525/elementa.2022.00103

Domain Editor-in-Chief: Jody W. Deming, University of Washington, Seattle, WA, USA

Associate Editor: Stephen F. Ackley, Department of Geological Sciences, University of Texas at San Antonio, TX, USA

Knowledge Domain: Ocean Science

Part of an Elementa Special Feature: The Multidisciplinary Drifting Observatory for the Study of Arctic Climate (MOSAiC)

Published: April 6, 2023 **Accepted:** February 1, 2023 **Submitted:** August 5, 2022

ELEMENTA Science of the Anthropocene

Elem Sci Anth is a peer-reviewed open access journal published by University of California Press.

OPEN ACCESS